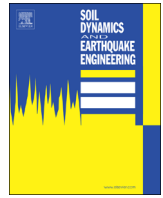




ELSEVIER

Contents lists available at ScienceDirect

Soil Dynamics and Earthquake Engineering

journal homepage: www.elsevier.com/locate/soildyn

The dynamic response of fluid-saturated porous materials with application to seismically induced soil liquefaction

Y. Heider^a, O. Avci^a, B. Markert^{b,*}, W. Ehlers^a

^a Institute of Applied Mechanics (CE), University of Stuttgart, Pfaffenwaldring 7, 70569 Stuttgart, Germany

^b Institute of General Mechanics, RWTH Aachen University, 52056 Aachen, Germany

ARTICLE INFO

Article history:

Received 25 April 2013

Received in revised form

18 October 2013

Accepted 29 March 2014

Keywords:

Porous media dynamics

Coupled problems

Flow liquefaction

Cyclic mobility

Elasto-viscoplasticity

TPM

FEM

ABSTRACT

The numerical simulation of liquefaction phenomena in fluid-saturated porous materials within a continuum-mechanical framework is the aim of this contribution. This is achieved by exploiting the Theory of Porous Media (TPM) together with thermodynamically consistent elasto-viscoplastic constitutive laws. Additionally, the Finite Element Method (FEM) besides monolithic time-stepping schemes is used for the numerical treatment of the arising coupled multi-field problem. Within an isothermal and geometrically linear framework, the focus is on fully saturated biphasic materials with incompressible and immiscible phases. Thus, one is concerned with the class of volumetrically coupled problems involving a potentially strong coupling of the solid and fluid momentum balance equations and the algebraic incompressibility constraint. Applying the suggested material model, two important liquefaction-related incidents in porous media dynamics, namely the flow liquefaction and the cyclic mobility, are addressed, and a seismic soil–structure interaction problem to reveal the aforementioned two behaviors in saturated soils is introduced.

© 2014 Elsevier Ltd. All rights reserved.

1. Introduction

The tendency of saturated porous materials to liquefy under the impact of dynamic loading is of a great importance especially in the fields of geomechanics, coastal engineering and seismology. As examples, consider the hazardous impacts of the seismically-induced liquefaction in offshore areas and near bodies of water or the wave-induced soil liquefaction under and around marine structures.

For the theoretical description of different physical phenomena in porous materials, the use of multiphase continuum mechanics is a standard practice. In this regard, when biphasic porous media like water-saturated soils are concerned, the Theory of Porous Media (TPM) is proven to provide a comprehensive and elaborated macroscopic modeling framework. Thereby, fluid-saturated materials are treated as multiphase aggregates consisting of solid and fluid constituents, which, independent of their usually unknown microtopology, are assumed to be in a state of ideal disarrangement over a representative elementary volume (REV). Applying a homogenization process to the REV yields a smeared-out averaged continuum model with overlapped, statistically distributed and interacting solid–fluid

aggregates. This way of treating multiphase porous materials can be traced back to the Theory of Mixtures (TM), cf. Bowen [8] or Truesdell and Toupin [76], where the TM was extended later by the concept of volume fractions to additionally incorporate information about the local composition of the homogenized continuum (cf. Goodman and Cowin [39]), which is fundamental to the TPM. This approach has been employed by Drumheller [24] to describe an empty porous solid. Bowen [9,10] extended this study to fluid-saturated porous media considering compressible as well as incompressible constituents. Subsequent developments of the TPM are mainly related to geomechanical investigations and have substantially been contributed by the works of de Boer and Ehlers, see [16,31,30] for detailed references.

Another popular macroscopic approach to model porous materials, which is based on a generalization of the theory of elasticity, is Biot's Theory (BT) introduced in the early works of Biot [5,6]. In fact, the BT and the TPM share a number of important features and yield the same results in particular cases. However, two intrinsic differences between them are important to be mentioned: first, unlike the TPM, the BT does not require that the constitutive laws fulfill the thermodynamic constraints. Second, BT treats sealed pores as a part of the solid phase, whereas the TPM assumes that all pores are interconnected. This leads to differences in the definition of constituent volume fractions and the partial densities, see, e.g., Schanz and Diebels [71] or Steeb [74] for quantitative and

* Corresponding author.

E-mail address: markert@iam.rwth-aachen.de (B. Markert).

detailed comparisons between the two mentioned approaches. In the literature, BT, the TM, and the TPM are considered as the bases of many works in the modeling of porous media dynamics, see Zienkiewicz et al. [78,79], Diebels and Ehlers [22], Lewis and Schrefler [54], Breuer [11] and Coussy [14] among others.

In the current treatment of fluid-saturated biphasic aggregates, the compressibility of the solid constituent is neglected in favor of the solid matrix compressibility. The pore fluid is also considered materially incompressible and the degree of saturation is 100%. This choice helps to concentrate on the aim of this paper in showing the ability of the considered constitutive model to capture different liquefaction-conjugate soil behaviors, such as the shear strength reduction, the development of the plastic volumetric strain and the accumulation of the pore pressure, and not to simulating a particular soil taken from a construction site. For real problems, choosing an incompressible pore fluid could overestimate the accumulated pore pressure as given in, e.g., Magda [56] or Okamura and Soga [66]. Moreover, this choice has impacts on the structure of the governing balance relations of biphasic porous materials. Considering a compressible pore fluid, a constitutive evolution equation for the pressure variable exists yielding a coupled system of ordinary differential equations (ODE). For a materially incompressible pore fluid, the time derivative of the pore pressure vanishes and the governing equations turn to be differential-algebraic equations (DAE) with singular generalized mass matrix, which can only be solved using special time integration schemes, see Markert et al. [61] or Zienkiewicz et al. [79] for a detailed discussion.

In talking about the response of structures founded on saturated soils, foundation soil affects the structural behavior during dynamic excitation (e.g., due to earthquakes) in two significant ways: by transmitting the ground motion in a form of applied dynamic loadings (a wave propagation problem), and by imposing permanent deformations caused by collapse of the underlying soils (a soil liquefaction problem). The response of the soil skeleton for the modeling of dynamic wave propagation is usually considered linear elastic and is governed by the Hookean elasticity law. In this regard, three apparent types of bulk waves are generally expected to propagate in a saturated porous medium: (1) The fast and weakly damped compressional waves (p_1) with an in-phase motion of the solid and fluid constituents. The appearance of this type of waves is mainly governed by the compressibility of the constituents, which in the case of the materially incompressible two-phase model yields a theoretically infinite propagation speed. (2) The slow (p_2 or Biot) longitudinal waves with out-of-phase motion of solid and fluid. In the case of a materially incompressible pore fluid, the appearance of the p_2 -wave is mainly governed by the deformability of the solid skeleton. (3) The transverse shear waves (s) are transmitted only in the solid skeleton and are mainly governed by its shear stiffness. For more details, we refer to the works of Biot [6,7], Heider et al. [47], Markert et al. [61] and Steeb et al. [75] among others.

For simulation of liquefaction events in saturated porous materials, the solid constituent response is treated in this work within an elasto-viscoplastic framework. This comprises the implementation of a hyperelastic model for the nonlinear elastic solid behavior (cf. Ehlers and Avcı [32], Müllerschon [63] and Scholz [73]), and also the application of the single-surface yield function of Ehlers [28,29] for capturing the plastic response. The viscosity in this model is mainly added to the elasto-plasticity treatment in order to improve the numerical stability of strain-localization problems and to reduce the mesh-dependency of the solution. In this, the viscosity parameters of sandy soils, which could be obtained from evaluation of experimental tests, are usually not sufficient to attain the aim of regularized solutions, and thus, higher viscosity parameters are used in the numerical

simulations, see, e.g. di Prisco and Imposimato [21] and Scholz [73] for more details.

The definitions and terminology of liquefaction-related phenomena are based on important publications in the fields of computational geomechanics and earthquake engineering such as the works by Castro [13], Ishihara et al. [49], Verdugo and Ishihara [77], Zienkiewicz et al. [79], Kramer and Elgamal [52] and de Groot et al. [20]. In this connection, liquefaction in saturated biphasic media is characterized by accumulation of the pore-fluid pressure and softening of the solid granular structure. Such behavior comprises a number of physical events such as the ‘flow liquefaction’ that appears in loose cohesionless soils and the ‘cyclic mobility’ that usually occurs in medium-dense to dense cohesionless soils, see Section 5 for details.

In the literature, a number of constitutive models have been devoted to simulate the response of granular materials under shear stress, which leads to volumetric strains under drained conditions and a build-up of the pore-fluid pressure under undrained conditions. In the realm of the plasticity theory and within the critical state framework, the Cam-Clay model [70] and the modified version of it are eligible to capture different liquefaction-conjugate soil behaviors. The complex and eventually anisotropic response of porous materials under dynamic loading required the development of more advanced material models. As examples, consider the bounding surface model (see, [55]) and the two-surface plasticity model as discussed in Manzari and Dafalias [58].

Another approach to soil liquefaction modeling, which is mainly based on phenomenological observations, is the densification model, cf., e.g. Zienkiewicz et al. [80,79] and Pastor et al. [67]. With this model and its modifications the densification of soil under cyclic loading, which leads to build-up of the pore-water pressure under undrained conditions, can be simulated. In this case, it is necessary to distinguish between the loading and the unloading stages, as well as to define a damage parameter to capture the dilatancy of soil. Besides the densification model, the relatively recent theory of hypoplasticity shows an increase in popularity in the field of soil dynamics modeling among other fields of geomechanics. The hypoplasticity is an incrementally nonlinear material model, which does not require the existence of a yield surface or the distinction between elastic and plastic strain increments. For details about this theory and its empirical extensions, see, e.g., Kolymbas [51] and Niemunis [64].

To give a brief overview of the topics in this paper, Section 2 describes the basics of the Theory of Porous Media, the concept of volume fractions, the kinematics of multiphase continua as well as the governing balance relations. In Section 3, thermodynamically consistent constitutive laws, which are able to describe various behaviors of the biphasic porous material, are presented. This includes the introduction of the nonlinear hyperelastic and the viscoplastic material models. Section 4 is concerned with the numerical treatment of the coupled problem, including the derivation of the weak formulation as well as the spatial and temporal discretization. Section 5 focuses on the investigation of liquefaction phenomena in saturated granular materials. In this, the basic features of liquefaction events like the pore-pressure build-up and the softening of the granular structure are figured out using a well-formulated elasto-viscoplastic constitutive model with isotropic hardening. A number of important factors that affect the response of saturated porous media, such as the loading rate and the boundary drainage, are discussed on the basis of a canonical initial-boundary-value problem (IBVP) in Section 6. The discussed constitutive formulations and schemes are applied in Section 7 to solve a realistic soil–structure interaction problem, which helps to illustrate the occurrence of seismically induced liquefaction events. Finally, Section 8 gives a brief summary and conclusions of the presented research work.

2. Theoretical basics

This section briefly introduces some of the fundamentals of multiphasic continuum theories. This includes the basic concepts of the TPM, the kinematics of multiphasic media and the balance relations in a specific form. The mathematical modeling is completed in Section 3 by introducing thermodynamically consistent constitutive relations, which are able to capture the material responses under different loading conditions. For a detailed discussion, the interested reader is referred to, e.g., [18,30,46,61].

2.1. Theory of porous media (TPM)

The TPM provides a comprehensive and excellent framework for the macroscopic modeling of a biphasic porous body consisting of an immiscible solid skeleton saturated by a single interstitial fluid. In this regard, the heterogeneous solid aggregate with a random granular geometry is assumed to be in a state of ideal disarrangement over a representative elementary volume (REV). Applying a homogenization process to the REV yields a smeared-out continuum φ with overlapped, interacting and statistically distributed solid and fluid aggregates φ^α ($\alpha = S$ for solid phase and $\alpha = F$ for pore-fluid phase). Thus, at any given macroscopic point, the relation $\varphi = \varphi^S \cup \varphi^F$ holds (see, Fig. 1).

Under the assumption of immiscible aggregates, the concept of volume fractions is introduced in order to integrate constituent microscopic information. Thus, a volumetric averaging process of all constituents is prescribed over the REV, and the incorporated physical fields of the micro-structure are represented by their local volume proportions. In particular, the volume fraction $n^\alpha := dv^\alpha / dv$ of φ^α is defined as the ratio of the partial volume element dv^α to the total volume element dv of φ . The saturation constraint for the case of a fully saturated medium is given by

$$\sum_{\alpha} n^{\alpha} = n^S + n^F = 1 \quad \text{with} \quad \begin{cases} n^S & : \text{solidity,} \\ n^F & : \text{porosity,} \end{cases} \quad (1)$$

and is assumed to be satisfied during the whole deformation process. The introduction of n^α is furthermore associated with two density functions, namely a material (effective or intrinsic) density $\rho^{\alpha R} := dm^\alpha / dv^\alpha$ and a partial density $\rho^\alpha := dm^\alpha / dv$, with dm^α being the local mass of φ^α . It is easily concluded that $\rho^\alpha = n^\alpha \rho^{\alpha R}$ underlines the general compressibility of porous solids under drained conditions through possible changes of the volume fractions, although the solid phase is materially incompressible.

2.2. Kinematics of multi-phase continua

In this work, the finite deformation kinematics is merely introduced as bases for the derivation of the small-strain relations, whereas the numerical modeling is restricted to the geometrically linear framework. In the multiphasic continuum mechanics (cf. [8]), one makes use of the concept of superimposed continua with internal interactions and individual states of motion. In this, the motion of a two-phase solid-fluid body is studied on the continuum level, where

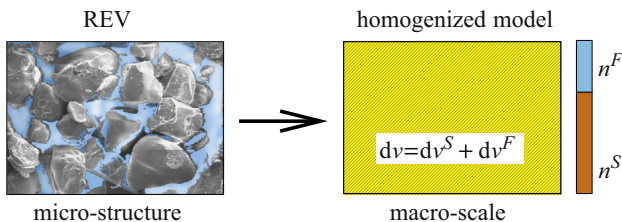


Fig. 1. REV of saturated sand showing the granular micro-structure and the biphasic TPM macro model with $\varphi = \varphi^S \cup \varphi^F$.

each of the constituents φ^α is supposed to occupy a considerable physical space of the overall homogenized body \mathcal{B} . Moreover, each constituent φ^α is represented by material points \mathcal{P}^α , which have unique positions \mathbf{X}_α in the reference configuration. In the actual configuration, each spatial position \mathbf{x} is occupied by one material point of each constituent, where the idea of superimposed and interacting continua with an exclusive motion function χ_α for each φ^α should be maintained, see Fig. 2 for illustration.

Following this, the Lagrangian (material) description of the current position, the velocity, and the acceleration of each constituent, respectively, is given in terms of unique motion (mapping) functions χ_α as

$$\begin{aligned} \mathbf{x} &= \chi_\alpha(\mathbf{X}_\alpha, t) \Leftrightarrow \mathbf{X}_\alpha = \chi_\alpha^{-1}(\mathbf{x}, t) \\ \mathbf{v}_\alpha &:= \dot{\mathbf{x}}_\alpha = \frac{d_\alpha \mathbf{x}}{dt}, \quad (\mathbf{v}_\alpha)_\alpha := \dot{\mathbf{x}}_\alpha = \frac{d_\alpha^2 \mathbf{x}}{dt^2}. \end{aligned} \quad (2)$$

Therein, χ_α^{-1} represents the unique inverse (Eulerian or spatial) motion function and

$$(\bullet)_\alpha' := \frac{d_\alpha(\bullet)}{dt} = \frac{\partial(\bullet)}{\partial t} + \text{grad}(\bullet) \mathbf{v}_\alpha \quad (3)$$

indicates the material time derivative of a vector-valued quantity (\bullet) following the motion of φ^α . Herein, $\text{grad}(\bullet) := \partial(\bullet) / \partial \mathbf{x}$ is the gradient operator, which is defined as the partial derivative of (\bullet) with respect to the local position \mathbf{x} . In the treatment of porous media dynamics, it is convenient to proceed from a Lagrangian description of the solid matrix via the solid displacement \mathbf{u}_S and the velocity \mathbf{v}_S as the kinematic variables. Moreover, the pore-fluid flow can be expressed either in a modified Eulerian setting via the seepage velocity vector \mathbf{w}_F describing the fluid motion relative to the deforming skeleton, or by an Eulerian description using the fluid velocity \mathbf{v}_F itself. In particular,

$$\begin{aligned} \mathbf{u}_S &= \mathbf{x} - \mathbf{X}_S, \quad \mathbf{v}_S = (\mathbf{u}_S)_S' = \dot{\mathbf{x}}_S, \\ \mathbf{v}_F &= \dot{\mathbf{x}}_F, \quad \mathbf{w}_F = \mathbf{v}_F - \mathbf{v}_S. \end{aligned} \quad (4)$$

Noting that in the governing balance relations used for the numerical treatment in Section 2.3, \mathbf{v}_F is adopted as the primary unknown for describing the pore-fluid motion and \mathbf{w}_F as a secondary variable. This choice has positive impacts on the numerical stability of the pore-pressure field in the case of a monolithic implicit time integration treatment, see [61] for detailed discussions. Back to Eq. (3), the material time derivative with respect to the fluid motion can be written as

$$(\bullet)_F' = (\bullet)_S' + \text{grad}(\bullet) \cdot \mathbf{w}_F, \quad (5)$$

where in the geometrically linear case, the nonlinear convective term can be omitted by magnitude arguments as $\text{grad}(\bullet) \cdot \mathbf{w}_F \ll (\bullet)_S'$ yielding $(\bullet)_F' \approx (\bullet)_S'$.

Following this, Eqs. (2) lead to the definition of the material deformation gradient \mathbf{F}_α and its inverse \mathbf{F}_α^{-1} as fundamental

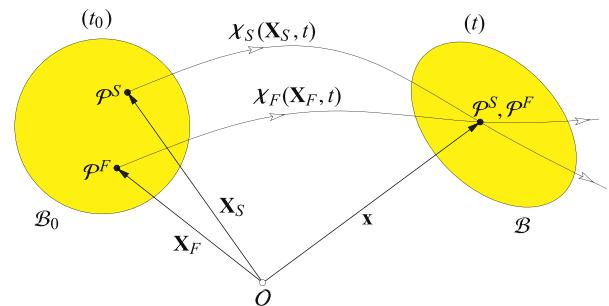


Fig. 2. Motion of a biphasic solid-fluid aggregate.

kinematic quantities in continuum mechanics. In particular,

$$\mathbf{F}_\alpha = \frac{\partial \mathbf{x}}{\partial \mathbf{X}_\alpha} =: \text{Grad}_\alpha \mathbf{x}, \quad \mathbf{F}_\alpha^{-1} = \frac{\partial \mathbf{X}_\alpha}{\partial \mathbf{x}} =: \text{grad } \mathbf{X}_\alpha \quad (6)$$

with $\text{Grad}_\alpha(\bullet) := \partial(\bullet)/\partial \mathbf{X}_\alpha$ denoting the gradient with respect to the reference position. In the finite deformation treatment of elasto-plasticity,² see, e.g., [26,27,44], a multiplicative split of the solid deformation gradient \mathbf{F}_S into an elastic \mathbf{F}_{Se} and a plastic \mathbf{F}_{Sp} part is introduced as

$$\mathbf{F}_S = \mathbf{F}_{Se} \mathbf{F}_{Sp}. \quad (7)$$

This property of \mathbf{F}_S will be used afterwards to split the solid volume fraction into an elastic and a plastic part. Moreover, similar to the additive decomposition of finite strain measures, such as the Green–Lagrangian strain \mathbf{E}_S of the reference configuration into an elastic (\mathbf{E}_{Se}) and a plastic (\mathbf{E}_{Sp}) term ($\mathbf{E}_S = \mathbf{E}_{Se} + \mathbf{E}_{Sp}$), an additive split of the small (linearized) strain tensor $\boldsymbol{\varepsilon}_S$ is adopted, viz.:

$$\mathbf{E}_{S \text{ lin}} := \boldsymbol{\varepsilon}_S = \frac{1}{2}(\text{grad } \mathbf{u}_S + \text{grad}^T \mathbf{u}_S) = \boldsymbol{\varepsilon}_{Se} + \boldsymbol{\varepsilon}_{Sp} \quad (8)$$

with $\boldsymbol{\varepsilon}_{Se}$ and $\boldsymbol{\varepsilon}_{Sp}$ being the elastic and the plastic small strain tensors, respectively.

2.3. Governing balance relations

The considered biphasic model excludes thermal effects as well as any mass exchanges (inert φ^α) and proceeds from intrinsically incompressible constituents ($\rho^{\alpha R} = \text{const.}$). In particular, the arising purely mechanical binary model with $\alpha = \{S, F\}$ is governed by the following constituent balance equations:

- Partial mass balance → partial volume balance:

$$(\rho^\alpha)'_\alpha + \rho^\alpha \text{div } \mathbf{v}_\alpha = 0 \rightarrow (n^\alpha)'_\alpha + n^\alpha \text{div } \mathbf{v}_\alpha = 0 \quad (9)$$

- Partial momentum balance:

$$\rho^\alpha (\mathbf{v}_\alpha)'_\alpha = \text{div } \mathbf{T}^\alpha + \rho^\alpha \mathbf{b} + \hat{\mathbf{p}}^\alpha \quad (10)$$

Herein, $\text{div}(\bullet)$ is the divergence operator related to $\text{grad}(\bullet)$, $\mathbf{T}^\alpha = (\mathbf{T}^\alpha)^T$ is the symmetric partial Cauchy stress assuming non-polar constituents, \mathbf{b} is the mass-specific body force acting on the overall aggregate, and $\hat{\mathbf{p}}^\alpha$ denotes the direct momentum production, which can be interpreted as the volume-specific local interaction force between the percolating pore fluid and the solid skeleton. Due to the overall conservation of momentum, $\hat{\mathbf{p}}^S + \hat{\mathbf{p}}^F = \mathbf{0}$ must hold for any closed multiphasic system. From Eq. (9) with $\alpha = S$ and $(n^S \rho^{SR})'_S = (n^S)'_S \rho^{SR}$, one directly obtains the solidity as a secondary variable by analytical integration:

$$(n^S)'_S = -n^S \text{div } \mathbf{v}_S \rightarrow n^S = n_{0S}^S (\det \mathbf{F}_S)^{-1} \quad (11)$$

with n_{0S}^S being the initial volume fraction of φ^S at time t_0 . Proceeding from the multiplicative geometric concept in (7), one introduces a plastic volume fraction n_p^S such that

$$n^S = n_p^S (\det \mathbf{F}_{Se})^{-1} \quad \text{with } n_p^S := n_{0S}^S (\det \mathbf{F}_{Sp})^{-1} \quad (12)$$

In the realm of the small strain theory, where

$$(\det \mathbf{F}_S)^{-1} \approx 1 - \text{div } \mathbf{u}_S \quad \text{and} \quad \text{div } \mathbf{u}_S = \boldsymbol{\varepsilon}_S \cdot \mathbf{I} := \boldsymbol{\varepsilon}_S^V \quad (13)$$

with $\boldsymbol{\varepsilon}_S$ according to Eq. (8), the linearized solidity reads

$$n^S = n_p^S (1 - \boldsymbol{\varepsilon}_{Se}^V) \quad \text{with } n_p^S := n_{0S}^S (1 - \boldsymbol{\varepsilon}_{Sp}^V) \quad (14)$$

Herein, $\boldsymbol{\varepsilon}_S^V = \boldsymbol{\varepsilon}_{Se}^V + \boldsymbol{\varepsilon}_{Sp}^V$ are the total, elastic and plastic volumetric strains, and n_p^S describes the permanent local solid volume changes associated with the evolution of the plastic intermediate configuration, see [57].

According to the principle of effective stresses, \mathbf{T}^α and $\hat{\mathbf{p}}^F$ can be split into effective field quantities, the so-called extra terms indicated by the subscript $(\bullet)_E$, and terms that are governed by the pore-fluid pressure p (see [19]):

$$\mathbf{T}^\alpha = \mathbf{T}_E^\alpha - n^\alpha p \mathbf{I}, \quad \hat{\mathbf{p}}^F = \hat{\mathbf{p}}_E^F + p \text{grad } n^F \quad (15)$$

with \mathbf{I} being the 2nd-order identity tensor. With regard to a thermodynamically consistent model, admissible constitutive equations for the response functions \mathbf{T}_E^α and $\hat{\mathbf{p}}_E^F$ must be provided.

It follows from a dimensional analysis that in a macroscopic porous media approach $\text{div } \mathbf{T}_E^F \ll \hat{\mathbf{p}}_E^F$ (cf. [23,43]), which yields in a good approximation that $\mathbf{T}^F \approx -n^F p \mathbf{I}$. The solid effective stress \mathbf{T}_E^S within the geometrically linear treatment will be referred to as $\boldsymbol{\sigma}_E^S$. Furthermore, under the assumption of isotropic lingering flow conditions at low Reynolds numbers, the percolation process is appropriately described by a linear Darcy-type filter law, which can be traced back to the simple but thermodynamically consistent relation

$$\hat{\mathbf{p}}_E^F = -\frac{(n^F)^2 \gamma^{FR}}{k^F} \mathbf{w}_F, \quad (16)$$

where $k^F > 0$ denotes the conventional hydraulic conductivity (Darcy permeability) in length/time and $\gamma^{FR} = \rho^{FR} g$ is the effective fluid weight with $g = |\mathbf{b}| = \text{const.}$ as the scalar gravitational acceleration.

In summary, the constituent balance equations (9) and (10) together with the constitutive and the kinematic relations yield the ‘convectiveless’ governing set of coupled partial differential equations (PDE):

- Momentum balance of the overall aggregate:

$$\rho^S (\mathbf{v}_S)'_S + \rho^F (\mathbf{v}_F)'_S = \text{div}(\boldsymbol{\sigma}_E^S - p \mathbf{I}) + (\rho^S + \rho^F) \mathbf{b}. \quad (17)$$

- Momentum balance of the pore fluid:

$$\rho^F (\mathbf{v}_F)'_S = -n^F \text{grad } p + \rho^F \mathbf{b} - \frac{(n^F)^2 \gamma^{FR}}{k^F} \mathbf{w}_F. \quad (18)$$

- Volume balance of the overall aggregate:

$$\text{div} \left(\mathbf{v}_S + \underbrace{\frac{k^F}{g} (\mathbf{b} - (\mathbf{v}_F)'_S) - \frac{k^F}{\gamma^{FR}} \text{grad } p}_{n^F \mathbf{w}_F} \right) = 0. \quad (19)$$

Note that the chosen primary unknowns for this set of PDE are \mathbf{u}_S , \mathbf{v}_F , and p . Hence, $\mathbf{v}_S(\mathbf{u}_S)$ as well as $\boldsymbol{\sigma}_E^S(\mathbf{u}_S)$, $n^S(\mathbf{u}_S)$, $n^F(\mathbf{u}_S)$, and \mathbf{w}_F represent secondary variables of the problem. Moreover, the fluid momentum balance (18) is solved with respect to the filter velocity $n^F \mathbf{w}_F$ and inserted into the volume balance of the overall aggregate (19). This modification guarantees that Eqs. (17)–(19) after spatial semi-discretization will yield a system of DAE with differential index 1, which is desirable for a smooth numerical solution. For particulars on index reduction methods, see, e.g., [3,42,60,61] among others. Additionally, a reduction in the order of the PDE to order one in time is achieved using

$$(\mathbf{u}_S)'_S = \mathbf{v}_S, \quad (20)$$

¹ The time derivatives within the small-strain framework are written with respect to the solid-phase motion $(\bullet)'_S$. However, as the convection term is neglected in the geometrically linear treatment, it is also possible to write them as partial time derivatives.

² The viscosity in the current treatment is added to the elasto-plastic model mainly due to numerical stability reasons and, thus, it is introduced as a constitutive approach in Section 3.2.

which eliminates the second time derivative of the solid displacement from Eq. (17) and allows the applicability of a wide range of time-stepping algorithms such as diagonal-implicit Runge Kutta (DIRK) methods, cf. [61].

3. Constitutive elasto-viscoplastic material modeling

In the following section, an elasto-viscoplastic material model for porous media within the framework of small deformations is discussed. Herein, the elastic behavior of the solid matrix is described via a nonlinear hyperelastic material model, see [32,37,73] for more details. The plastic behavior is captured using a single-surface yield function, see [28,29]. Additionally, this section briefly presents the non-associative flow rule and the isotropic hardening modeling.

3.1. Elastic material response

The elastic material behavior of sand is highly nonlinear during hydrostatic loading. This nonlinear elastic behavior is captured in this work using a hyperelastic material model, cf. [4,32,36,37,63,73]. The proposed elasticity model fulfills the thermodynamical restrictions and shows a very good performance in describing the elastic deformation of isotropic porous materials. Under the assumption of uncrushable solid particles, a maximum solid volume fraction (n_{\max}^S) is defined as a point of compaction (cf. [25,32]). The value of n_{\max}^S depends on the granular geometry and adds a restriction to the elastic volumetric strain. Here, the critical elastic volumetric strain $\epsilon_{Se,crit}^V$, associated with n_{\max}^S , is defined as

$$\epsilon_{Se,crit}^V = 1 - \frac{n_{\max}^S}{n_p^S} \quad \text{with } n^S \leq n_{\max}^S < 1. \quad (21)$$

Within a thermodynamical framework, the Helmholtz free-energy function ψ^S can be additively split into a purely elastic ψ^{Se} and an inelastic (plastic) ψ^{Sp} term. For the hyperelastic material model, the following expression can be used for the elastic free-energy density function, cf. [4,36]:

$$\rho_{0S}^S \psi^{Se} = \mu^S \mathbf{e}_{Se}^D \cdot \mathbf{e}_{Se}^D + \frac{1}{2} (k_0^S - k_1^S) (\epsilon_{Se}^V)^2 - k_1^S (\epsilon_{Se,crit}^V)^2 \left[\ln \left(\frac{\epsilon_{Se,crit}^V - \epsilon_{Se}^V}{\epsilon_{Se,crit}^V} \right) + \frac{\epsilon_{Se}^V}{\epsilon_{Se,crit}^V} \right]. \quad (22)$$

Herein, ρ_{0S}^S is the initial solid density, k_0^S and k_1^S govern the initial and the nonlinear bulk modulus of the solid skeleton, respectively, \mathbf{e}_{Se}^D is the elastic deviatoric strain,³ and μ^S is the macroscopic solid shear modulus (1st Lamé constant). Following this, the solid effective stress reads

$$\begin{aligned} \boldsymbol{\sigma}_E^S &= \rho_{0S}^S \frac{\partial \psi^{Se}}{\partial \mathbf{e}_{Se}^D} \\ &= 2\mu^S \mathbf{e}_{Se}^D + \left[k_0^S + k_1^S \left(\frac{\epsilon_{Se,crit}^V}{\epsilon_{Se,crit}^V - \epsilon_{Se}^V} - 1 \right) \right] \epsilon_{Se}^V \mathbf{I}. \end{aligned} \quad (23)$$

In Eq. (23), the elastic deviatoric stress is considered to be linear and governed by a constant shear modulus μ^S , whereas the hydrostatic part of $\boldsymbol{\sigma}_E^S$ has been chosen to simulate the highly nonlinear unloading–reloading hydrostatic response.⁴

3.2. Plastic material response

In the following, a single-surface plasticity model within the elasto-viscoplasticity framework together with an isotropic hardening law is

applied to simulate different behaviors of saturated soils under dynamic loading. The components of the considered plasticity treatment can be distinguished as follows: (1) the yield function that encompasses the elastic domain, (2) the non-associative flow rule that describes the evolution of the plastic strain and the loading/unloading criterion in order to differentiate between the elastic and the plastic steps, and (3) the hardening/softening and failure states, where an isotropic hardening model is introduced to describe the expansion/contraction of the yield surface. The considered yield surface is defined in the principal stress space as shown in Fig. 3.

As granular materials exhibit volumetric as well as deviatoric plastic deformations, the yield surface should have a closed shape and be a function of the first stress invariant I_σ that represents the hydrostatic confining stress. In particular, the yield function is given in terms of the first principal stress invariant I_σ as well as the second and the third deviatoric stress invariants $\Pi_\sigma^D, \text{III}_\sigma^D$ as

$$F(\boldsymbol{\sigma}_E^S) = \sqrt{\Phi} + \beta I_\sigma + \epsilon I_\sigma^2 - \kappa = 0$$

with

$$\Phi = \Pi_\sigma^D \left(1 + \gamma \frac{\text{III}_\sigma^D}{(\Pi_\sigma^D)^{3/2}} \right)^m + \frac{1}{2} \alpha I_\sigma^2 + \delta^2 I_\sigma^4. \quad (24)$$

Therein, the stress invariants are defined as

$$\begin{aligned} I_\sigma &= \boldsymbol{\sigma}_E^S \cdot \mathbf{I}, \\ \Pi_\sigma^D &= \frac{1}{2} (\boldsymbol{\sigma}_E^S)^D \cdot (\boldsymbol{\sigma}_E^S)^D, \\ \text{III}_\sigma^D &= \frac{1}{3} (\boldsymbol{\sigma}_E^S)^D \cdot (\boldsymbol{\sigma}_E^S)^D \cdot (\boldsymbol{\sigma}_E^S)^D. \end{aligned} \quad (25)$$

The yield surface is also a function of two sets of material parameters, namely, the hydrostatic parameters $S_h = \{\alpha, \beta, \delta, \epsilon, \kappa\}$, which control the shape of the yield surface in the hydrostatic plane, and the deviatoric variables $S_d = \{\gamma, m\}$, which define the shape of F in the deviatoric plane, see [29,32,36] for details.

Adoption of an associative flow rule with plastic flow direction perpendicular to the yield surface obviously leads to an over-estimation of the plastic dilation behavior. Therefore, a non-associative flow rule needs to be formulated by introducing a plastic potential function different from the yield function. In this connection, the following potential relation as a function of the first principal stress invariant I_σ and the second deviatoric stress invariant Π_σ^D is suggested (cf. [57]):

$$\begin{aligned} G(\boldsymbol{\sigma}_E^S) &= \sqrt{\psi_1 \Pi_\sigma^D + \frac{1}{2} \alpha I_\sigma^2 + \delta^2 I_\sigma^4} \\ &\quad + \psi_2 \beta I_\sigma + \epsilon I_\sigma^2 - \kappa \end{aligned} \quad (26)$$

with ψ_1, ψ_2 being additional parameters for adjusting the plastic dilation angle.

Following this, a constitutive equation for the temporal evolution of \mathbf{e}_{Sp} needs to be specified. Therefore, based on the Principle

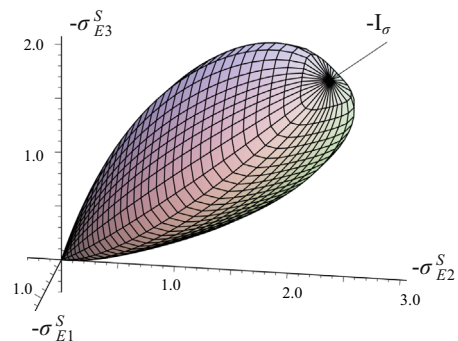


Fig. 3. Single-surface yield function in the principal stress space, cf. [28].

³ For a 2nd-order tensor \mathbf{A} , the deviatoric part reads $\mathbf{A}^D = \mathbf{A} - \frac{1}{3}(\mathbf{A} \cdot \mathbf{I})\mathbf{I}$.

⁴ Comparing the introduced nonlinear elasticity law with the Hookean elasticity law ($\boldsymbol{\sigma}_E^S = 2\mu^S \mathbf{e}_S + \lambda^S (\mathbf{e}_S \cdot \mathbf{I})\mathbf{I}$), both have a linear deviatoric stress part and the 2nd Lamé constant λ^S is associated with k_0^S .

of Maximum Dissipation (PMD), a dissipative optimization problem is formulated within the potential surface leading to a canonical formulation for $(\boldsymbol{\epsilon}_{sp})'_S$. In particular, the *flow rule* can be expressed as

$$(\boldsymbol{\epsilon}_{sp})'_S = \Lambda \frac{\partial G}{\partial \boldsymbol{\sigma}_E^S} \quad (27)$$

with Λ being the plastic multiplier. A necessary condition for the solution of the problem in Eq. (27) is the Karush–Kuhn–Tucker (KKT) optimality condition, which can be expressed for the case of rate-independent elasto-plasticity as

$$F \leq 0, \quad \Lambda \geq 0, \quad \Lambda F = 0. \quad (28)$$

In the numerical implementation of rate-independent elasto-plasticity, instability and ill-posedness might be encountered during, e.g., shear band localization problems (mesh-dependent solution), cf. [34,65]. A possible method to overcome such a difficulty is to introduce an artificial rate-dependency by adding viscosity to the elasto-plastic model. According to the overstress concept of Perzyn [68], the following viscosity approach can be used:

$$\Lambda = \frac{1}{\eta_r} \left\langle \frac{F}{\sigma_0} \right\rangle^r. \quad (29)$$

Here, $\langle \cdot \rangle$ are the Macauley brackets defined as $\langle \cdot \rangle := \frac{1}{2}[(\cdot) + |(\cdot)|]$, σ_0 is a reference overstress, r is the viscoplastic exponent and η_r is the viscoplastic relaxation time. As the aim of the viscosity in this case is merely to improve the numerical stability, choosing a small value for η_r together with $\sigma_0 > 0$ and $r = 1$ allows for an elasto-viscoplastic model, which behaves very much similar to the elasto-plastic model but with better stability properties, see, e.g., [45,73] for more details.

Experiments on dry sand show that isotropic hardening effects appear instantly after loading in triaxial compression tests, whereas a softening behavior might be obtained for dense sand after reaching a certain stress peak. Such isotropic hardening and softening tendencies are related to the plastic deformations and can be well captured with the suggested constitutive model by introducing suitable evolution relations for a subset of the material parameters $p_i \in \{\beta, \delta, \epsilon, \gamma\}$ in the yield function. Hence, the parameters p_i are chosen as functions of the dissipative plastic work (cf. [17]). According to [36], the evolution relations for the parameters p_i are split into volumetric (p_i^V) and deviatoric (p_i^D) parts, viz.:

$$\begin{aligned} (p_i)'_S &= (p_i^V)'_S + (p_i^D)'_S \\ &= (\dot{p}_i^* - p_i)(C_{pi}^V (\boldsymbol{\epsilon}_{sp}^V)'_S + C_{pi}^D \|(\boldsymbol{\epsilon}_{sp}^D)'_S\|). \end{aligned} \quad (30)$$

In this, \dot{p}_i^* and $p_{i0} = p_i(t_0)$ are the maximum and the initial values of p_i , and C_{pi}^V, C_{pi}^D are material constants. The suggested relation (30) allows us to distinguish between a deviatoric, positive term $\|(\boldsymbol{\epsilon}_{sp}^D)'_S\|$ yielding a plastic hardening behavior, and a volumetric part that results in positive (hardening) or negative (softening) values. Thus, both the densification and the loosening behaviors of the granular structure are represented.

4. Numerical treatment of the coupled problem

For the numerical solution of an initial-boundary value problem, the FEM treatment is carried out in two steps: firstly, deriving the weak or variational statements of the governing balance equations and, secondly, using the finite element discretization for the approximate solution of the variational equations. In what follows, the governing set of partial differential balance equations (17)–(19) with primary unknowns $\mathbf{u}_S, \mathbf{v}_F, p$ is treated in a fully coupled manner and referred to as *uvp*-formulation.

Additionally, the secondary variable $\mathbf{v}_S(\mathbf{u}_S)$ given in (20) is considered together with the primary variables to reduce the order of the coupled equations into order one in time. Therefore, the vector of unknowns \mathbf{u} of the three-field problem can be written (in analogous to [47,61]) as

$$\mathbf{u} = \mathbf{u}(\mathbf{x}, t) \quad \text{with} \quad \mathbf{u} = [\mathbf{u}_S \quad \mathbf{v}_S \quad \mathbf{v}_F \quad p]^T. \quad (31)$$

4.1. Governing weak formulation

Following the common FEM procedure for deriving the weak formulation (cf. [81]), Eqs. (17)–(19) are weighted by independent test functions and integrated over the spatial domain Ω occupied by the overall aggregate body \mathcal{B} . Moreover, the boundary $\Gamma = \partial\Omega$ is split into Dirichlet (essential) and Neumann (natural) boundaries, respectively, yielding $\Gamma = \Gamma_{\mathbf{u}} \cup \Gamma_{\mathbf{t}}$ for the momentum balance of the overall aggregate, $\Gamma = \Gamma_{\mathbf{v}_F} \cup \Gamma_{\mathbf{t}^F}$ for the fluid momentum balance and $\Gamma = \Gamma_p \cup \Gamma_v$ for the volume balance of the overall aggregate. Next, applying the product rule and the Gaussian integral theorem, one obtains the weak forms of the *uvp*-formulation. In particular, the overall aggregate momentum balance in a weak form reads

$$\begin{aligned} \int_{\Omega} \text{grad } \delta \mathbf{u}_S \cdot (\boldsymbol{\sigma}_E^S - p \mathbf{I}) \, dv - \int_{\Gamma_{\mathbf{t}}} \delta \mathbf{u}_S \cdot \bar{\mathbf{t}} \, da \\ + \int_{\Omega} \delta \mathbf{u}_S \cdot \{\rho^S (\mathbf{v}_S)'_S + \rho^F (\mathbf{v}_F)'_S - \rho \mathbf{b}\} \, dv = 0 \end{aligned} \quad (32)$$

with $\delta \mathbf{u}_S$ being the test function corresponding to the primary variable \mathbf{u}_S or \mathbf{v}_S . Moreover, $\bar{\mathbf{t}} = (\boldsymbol{\sigma}_E^S - p \mathbf{I}) \mathbf{n}$ is the external load vector acting on the Neumann boundary $\Gamma_{\mathbf{t}}$ of the overall aggregate with outward-oriented unit surface normal \mathbf{n} .

The weak form of the fluid momentum balance can be expressed as

$$\begin{aligned} - \int_{\Omega} \text{div}(\delta \mathbf{v}_F) n^F p \, dv - \int_{\Gamma_{\mathbf{t}^F}} \delta \mathbf{v}_F \cdot \bar{\mathbf{t}}^F \, da \\ + \int_{\Omega} \delta \mathbf{v}_F \cdot \left\{ \rho^F \left[(\mathbf{v}_F)'_S - \mathbf{b} \right. \right. \\ \left. \left. + \left(\text{grad } \mathbf{v}_F + \frac{n^F g}{k^F} \mathbf{I} \right) (\mathbf{v}_F - \mathbf{v}_S) \right] \right\} \, dv = 0, \end{aligned} \quad (33)$$

where $\delta \mathbf{v}_F$ is the test function corresponding to the primary variable \mathbf{v}_F . Moreover, $\bar{\mathbf{t}}^F = -n^F p \mathbf{n}$ is the external fluid load vector acting on $\Gamma_{\mathbf{t}^F}$. The overall aggregate volume balance in a weak form reads

$$\begin{aligned} \int_{\Omega} \delta p \, \text{div } \mathbf{v}_S \, dv - \int_{\Omega} \text{grad } \delta p \cdot n^F (\mathbf{v}_F - \mathbf{v}_S) \, dv \\ + \int_{\Gamma_v} \delta p \, \bar{v} \, da = 0 \end{aligned} \quad (34)$$

with δp being the test function related to the primary variable p and $\bar{v} = n^F \mathbf{w}_F \cdot \mathbf{n}$ denotes the volume efflux of the incompressible fluid draining through the Neumann boundary Γ_v .

4.2. Spatial and temporal discretization

For the spatial semi-discretization, the continuous control space Ω occupied by the overall aggregate \mathcal{B} is subdivided into N_e finite elements yielding an approximate discrete domain Ω^h . This treatment yields a FE mesh with N_x nodes for the geometry approximation, on which the following discrete trial and test

functions are defined:

$$\begin{aligned} \mathbf{u}^h(\mathbf{x}, t) &= \bar{\mathbf{u}}^h(\mathbf{x}, t) + \sum_{i=1}^{N_u} \mathbf{N}_{u(i)}(\mathbf{x}) \mathbf{u}_{(i)}(t) \in \mathcal{S}_u^h(t) \\ \delta \mathbf{u}^h(\mathbf{x}) &= \sum_{i=1}^{M_u} \mathbf{M}_{u(i)}(\mathbf{x}) \delta \mathbf{u}_{(i)} \in \mathcal{T}_u^h. \end{aligned} \quad (35)$$

Therein, $\bar{\mathbf{u}}^h$ are the approximated Dirichlet boundary conditions of the considered problem, N_u denotes the number of FE nodes used for the approximation of the respective fields in \mathbf{u} , and $\mathbf{N}_{u(i)}$ represents the global basis functions at node i which depend only on the spatial position \mathbf{x} , whereas the degrees of freedom $\mathbf{u}_{(i)}$ are the time-dependent nodal coefficients. Moreover, M_u is the number of FE nodes used for the test functions $\delta \mathbf{u}_S$, $\delta \mathbf{v}_F$, and δp , respectively, $\mathbf{M}_{u(i)}$ denotes the global basis functions, and $\delta \mathbf{u}_{(i)}$ represents the corresponding nodal values of the test functions. Furthermore, $\mathcal{S}_u^h(t)$ and \mathcal{T}_u^h are the discrete, finite-dimensional trial and test spaces. In the current contribution, the Bubnov–Galerkin procedure is applied using the same basis functions $\mathbf{N}_{u(i)} \equiv \mathbf{M}_{u(i)}$ for the approximation of \mathbf{u} and $\delta \mathbf{u}$. For more details, the interested reader is referred to, e.g., [2,12,33,40,46,61].

The spatial discretization is applied to the weak formulations (32)–(34) and Eq. (20), which are collected in a function vector \mathcal{G}_u^h . The plasticity evolution relations (27) and (30) are also collected after spatial discretization in a function vector \mathcal{L}_q^h . Thus, let $\mathbf{y} = \mathbf{y}(t) = [\mathbf{u}_S \mathbf{v}_S \mathbf{v}_F \mathbf{p}]^T \in \mathbb{R}^m$ with $m = \dim(\mathbf{y})$ represent all nodal degrees of freedom $\mathbf{u}_{(i)}(t)$ of the FE mesh, and $\mathbf{q} = \mathbf{q}(t) = [e_{sp}^1, \dots, p_i]^T \in \mathbb{R}^n$ with $n = \dim(\mathbf{q})$ represent all internal variables at the integration points. Then, assembling the unknowns in one vector $\mathbf{z} := [\mathbf{y}, \mathbf{q}]^T \in \mathbb{R}^{m+n}$, one obtains an initial-value problem of differential-algebraic equations (DAE) in time in an abstract form as

$$\begin{aligned} \mathbf{F}(t, \mathbf{z}, (\mathbf{z}'_S)) &\equiv \begin{bmatrix} \mathcal{G}_u^h(t, \mathbf{y}, (\mathbf{y}'_S); \mathbf{q}) \\ \mathcal{L}_q^h(t, \mathbf{q}, (\mathbf{q}'_S); \mathbf{y}) \end{bmatrix} \\ &\equiv \begin{bmatrix} \mathbf{M}(\mathbf{y}'_S) + \mathbf{k}(\mathbf{y}; \mathbf{q}) - \mathbf{f} \\ \mathbf{A}(\mathbf{q}'_S) - \mathbf{l}(\mathbf{q}; \mathbf{y}) \end{bmatrix} \stackrel{!}{=} \mathbf{0}. \end{aligned} \quad (36)$$

Therein, \mathbf{M} denotes a generalized mass matrix, \mathbf{k} is a generalized stiffness vector, and \mathbf{f} is a generalized external force vector. The evolution relations \mathcal{L}_q^h in (36) represent ordinary differential equations (ODE), which are solved at every integration point of the finite element mesh. Herein, \mathbf{A} is an identity matrix and the vector \mathbf{l} contains the semi-discrete right-hand sides of the evolution equations, cf. [36,38,59].

For the considered case of materially incompressible solid and fluid aggregates, the global mass matrix is singular as it has no entry corresponding to the pore-pressure time derivative (\mathbf{p}'_S) (algebraic coupling), which implies that explicit monolithic schemes are not applicable. Hence, proceeding from a strongly coupled problem governed by realistic permeabilities $0 < k^F \leq 1$, monolithic implicit time-integration schemes can conveniently be applied, cf. [61]. In the case of monolithic solutions, Taylor-Hood-like elements are chosen for the FE treatment with quadratic approximations of \mathbf{u}_S and \mathbf{v}_S and linear approximations of \mathbf{v}_F and p , which fulfill the inf-sup or Ladyszenskaya–Babuška–Brezzi (LBB) stability condition (cf. [40] for references). In this paper, the resulting system of DAE is discretized in time using the monolithic implicit (Backward) Euler (BE) time-integration scheme, which is appropriate for first-order DAE systems and requires reasonable computational capacity. Choosing a sufficiently small time-step size in the solution of the dynamic problem helps to reduce the artificial numerical damping of the BE scheme, improves the accuracy in the case of a plastic strain evolution and guarantees that the dynamic excitation is accurately described, see [46].

5. Simulation of sand behavior under deviatoric stress

In the following, the elasto-viscoplastic constitutive model, as introduced in Section 3, is used to capture the basic behavior of saturated granular materials under shear stress, such as the pore-fluid pressure accumulation accompanied by a reduction of the effective stress. Thus, a number of liquefaction-related definitions and terminologies are briefly given, which are commonly used in the fields of soil modeling and earthquake engineering, see, e.g., [13,48,49,52,77,79] for more details. In this, *Liquefaction* is a general term used to describe the response of saturated soils, which is characterized by build-up of the pore pressure and softening of the granular structure. This comprises a number of physical phenomena such as the ‘flow liquefaction’ and the ‘cyclic mobility’. *Flow liquefaction* is an instability phenomenon that frequently happens in loose soils with low shear strength. Under undrained conditions the applied load results in an increase of the pore pressure and an incredible reduction of the mean effective stress until the residual shear strength cannot sustain the static equilibrium. Consequently, saturated soil loses its nature as a solid and flows like a viscous fluid. *Cyclic mobility* is a kind of permanent but limited plastic deformation of saturated soil under cyclic shear loading. Herein, an accumulation of the pore pressure takes place after each applied cycle, however, the mean effective stress can never reach a zero value, and the residual shear strength can always maintain the static equilibrium.

5.1. Capturing the contractive and dilative behaviors

The initial density of sand plays a key role in the response to shear stress, cf. [20,52]. Under deviatoric stress in consolidated drained triaxial tests (CD), a dense granular assemblage is expected to compact and then to dilate, whereas a very loose assemblage tends more likely to compact until collapse. In consolidated undrained triaxial tests (CU), it is assumed that the samples are 100% saturated with a materially incompressible fluid and no drainage occurs. Therefore, the contraction tendency leads to a build-up of the pore pressure, whereas the dilation tendency causes an opposing response.

In the current modeling, a non-associative flow rule for the plastic material behavior is applied, cf. Section 3. In this, the plastic potential function in Eq. (26) and its parameters ψ_1, ψ_2 play a decisive role in the realization of the contractive and dilative behaviors. In the following, a sand with four different initial densities (Table 1) is investigated, whereas the values of ψ_1 and ψ_2 for the numerical applications are given in Table A3.

As a measure for the flow direction, the dilatancy angle ν is introduced, cf. [28,29,63]

$$\tan \nu := \frac{\mathbf{l}(\mathbf{e}_{sp})'_S}{\|(\mathbf{e}_{sp}^D)'_S\|} = \frac{(\mathbf{e}_{sp})'_S \cdot \mathbf{I}}{\sqrt{(\mathbf{e}_{sp}^D)'_S \cdot (\mathbf{e}_{sp}^D)'_S}} \quad (37)$$

If $(\mathbf{e}_{sp}^D)'_S \cdot \mathbf{I} > 0$, the behavior is dilative and the volumetric strain increases, whereas if $(\mathbf{e}_{sp}^D)'_S \cdot \mathbf{I} < 0$, the volumetric strain decreases

Table 1

A sand with different initial densities, where the classifications are based on the relative density $Dr := (n_{0S}^s - n_{\min}^s) / (n_{\max}^s - n_{\min}^s) \times 100\%$.

Initial density	Dr (%)	Description w.r.t.	Dr (%)
Case (1)	95	Very dense	> 75
Case (2)	56	Dense	50–75
Case (3)	33	Moderate dense	30–50
Case (4)	9.5	Very loose	< 15

and the behavior is contractive. If $(\mathbf{e}_{Sp}^D)'_S \cdot \mathbf{I} = 0$, the material deforms at a constant volumetric strain.

5.2. Pore-pressure accumulation and dissipation

For the treatment of the pore-pressure accumulation and dissipation, some basic concepts of soil mechanics are recalled. Here, the effective stress relations (15)₁ for a biphasic material can be rewritten as

$$\boldsymbol{\sigma} = \boldsymbol{\sigma}_E^S - p\mathbf{I} \tag{38}$$

with $\boldsymbol{\sigma}$ as the total stress in the geometric linear treatment. Eq. (38) can be further reformulated by use of the mean stress $\sigma_m := \frac{1}{3} \text{tr} \boldsymbol{\sigma}$ and the mean effective stress $\sigma_{E,m}^S := \frac{1}{3} \text{tr} \boldsymbol{\sigma}_E^S$ as scalar quantities yielding

$$\sigma_m = \sigma_{E,m}^S - p, \tag{39}$$

where the trace of a tensor (\bullet) is defined as $\text{tr}(\bullet) = (\bullet) \cdot \mathbf{I}$. In the absence of a sudden excitation (or under quasi-static loading), each grain of the soil particle assemblage is found in contact with a number of neighboring particles, which allows the solid skeleton to carry most of the applied external total stress ($\boldsymbol{\sigma} \approx \boldsymbol{\sigma}_E^S$ and $p \approx 0$). Under rapidly applied loading of a loose, saturated granular material, the applied external stress is mostly carried by the pore fluid leading to a poor contact between the solid grains, which causes a softening of the granular deposit ($\sigma_{E,m}^S \approx 0$). Thereafter, the excess pore-fluid pressure starts to dissipate, which causes an adverse motion of the solid and the pore fluid phases. This process can be explained based on macroscopic filter law, which results from the overall momentum balance (18) as

$$n^F \mathbf{w}_F = -\frac{k^F}{\gamma_{FR}} \text{grad } p + \frac{k^F}{g} [\mathbf{b} - (\mathbf{v}_F)'_S]. \tag{40}$$

In this, the permeability parameter k^F plays an important role in the rapidity of the excess pore-pressure dissipation.

5.3. Capturing the drained and undrained sand behaviors

The aim of the following numerical benchmark is to show the ability of the suggested material model (Section 3) to capture the behavior of sand in triaxial tests under drained and undrained conditions. The axisymmetric cylindrical triaxial test cell can be simplified into a two-dimensional (2-d) single-element problem with boundary conditions and loads illustrated in Fig. 4.

The material response is considered elasto-viscoplastic with the nonlinear elastic parameters given in Table A2 and the viscoplastic parameters in Table A4. In this connection, four cases of initial densities with four sets of dilatancy parameters are applied as given in Table A3. As a matter of fact, changing the

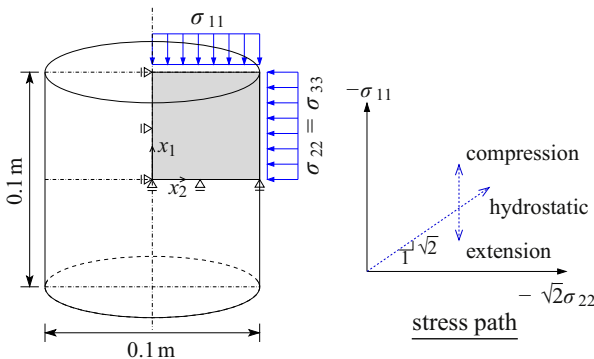


Fig. 4. Boundary conditions and applied loads of the triaxial test. Simplification of the axisymmetric 3-d problem into a 2-d problem.

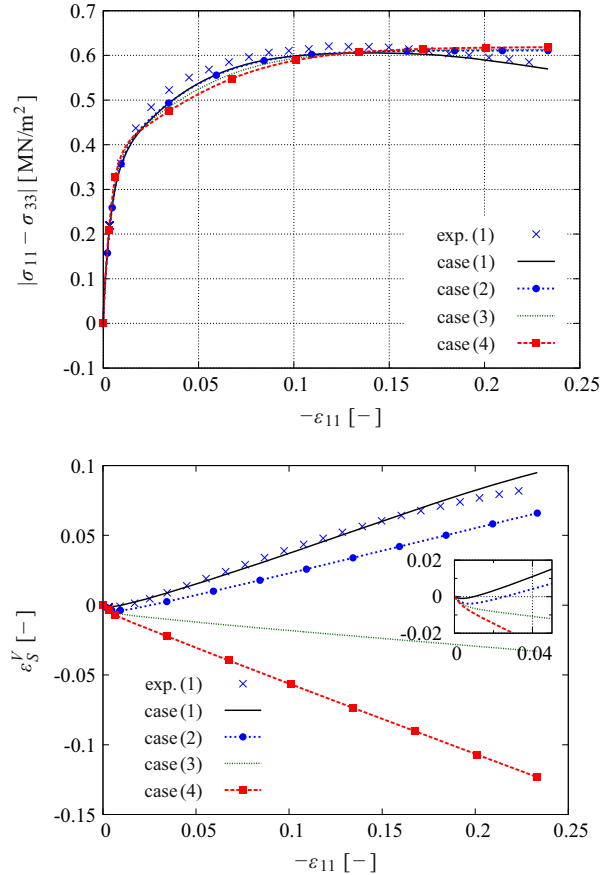


Fig. 5. Experimental and numerical results of the drained compression triaxial test for the different parameter cases in Table A3.

initial density affects the overall sand behavior, which requires basically the modification of many parameters of the model to capture the accurate response. However, this is beyond the scope of this publication, which concentrates on describing the general granular behavior without calibrating a certain sand behavior. The parameters for case (1) have been obtained in the laboratory of the Institute of Applied Mechanics, University of Stuttgart, based on consolidated drained triaxial compression tests, cf. [32]. The parameters ψ_1 and ψ_2 for cases (2)–(4) have been chosen appropriately to demonstrate the change of response in accordance to the initial density.

The obtained CD triaxial test results between the axial strain ϵ_{11} and the deviatoric stress $|\sigma_{11} - \sigma_{33}|$ for cases (1)–(4) are depicted in Fig. 5. Therein, a good agreement between the experimental and the numerical results can be seen for case (1) of a very dense sand. In case (1), the deviatoric stress increases to a certain peak and then decreases as can be seen in Fig. 5, top. Moreover, Fig. 5, bottom, shows that the first part of the test undergoes a slight contraction until a minimum void ratio is attained. Thereafter, the material exposes a dilative behavior until collapse. For a very loose sand as in case (4), the contraction tendency is dominant and no peak in the deviatoric stress can be observed. Following this, it is shown that the tendency of the granular assemblage to contract increases by decreasing the initial density. Herein, the influence of the initial density on the behavior can numerically be encountered by choosing proper ψ_1 and ψ_2 parameters of the plastic potential function.

The numerical simulation of the consolidated undrained (CU) triaxial test with four cases of initial densities (cf. Table A3) is introduced in the following. The CU test for saturated sandy

materials is performed in two steps: (i) A drained consolidation step, where a hydrostatic compression is applied to the specimen. (ii) An undrained deviatoric step (displacement-controlled in our case), where a pore-pressure build-up is allowed to occur. Under monotonic loading, Fig. 6 shows that cases (1) and (2) of very dense to dense specimens experience a short period of contraction, which causes a slight increase of the pore-fluid pressure. This phase is followed by a continuous dilation leading to a decrease of the pore pressure and an increase of the mean effective stress.

Considering the specimens with moderate density in case (3), the initial response is contraction leading to an accumulation of the pore pressure, which is followed by a phase of immense increase of the axial strain accompanied by a slight change of the shear stress and the mean effective stress until collapse. This type of behaviors corresponds, according to the aforementioned definitions, to the cyclic mobility when the applied load is cyclic. Case (4) in Fig. 6 represents the flow liquefaction behavior. Therein, the very loose sample exhibits a peak deviatoric stress followed by a serious decrease of the shearing resistance and a continuous build-up of the pore pressure until the collapse is attained. According to [52], the latter behavior is reached due to the collapse of the soil skeleton structure.

The interplay between the mean effective stress and the excess pore pressure for cases (3) and (4) is governed by Eq. (39) and depicted in Fig. 7. For case (3) of moderate-dense specimens, Fig. 7, top, shows a transformation state between the contractive and the dilative phases, where the excess pore pressure and the effective stress reverse their behaviors. In the dilative tendency stage, the applied load

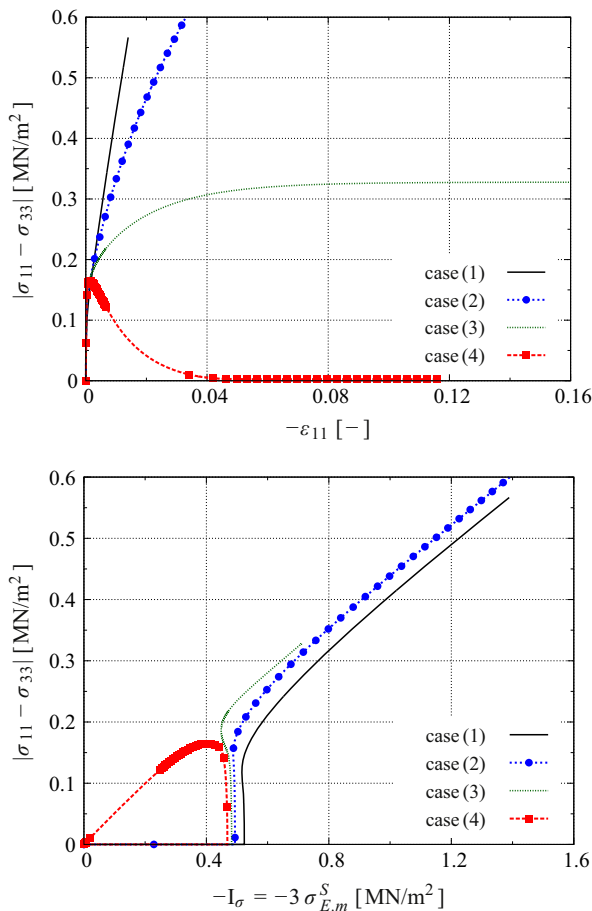


Fig. 6. Numerical results of undrained triaxial compression tests for the different cases in Table A3.

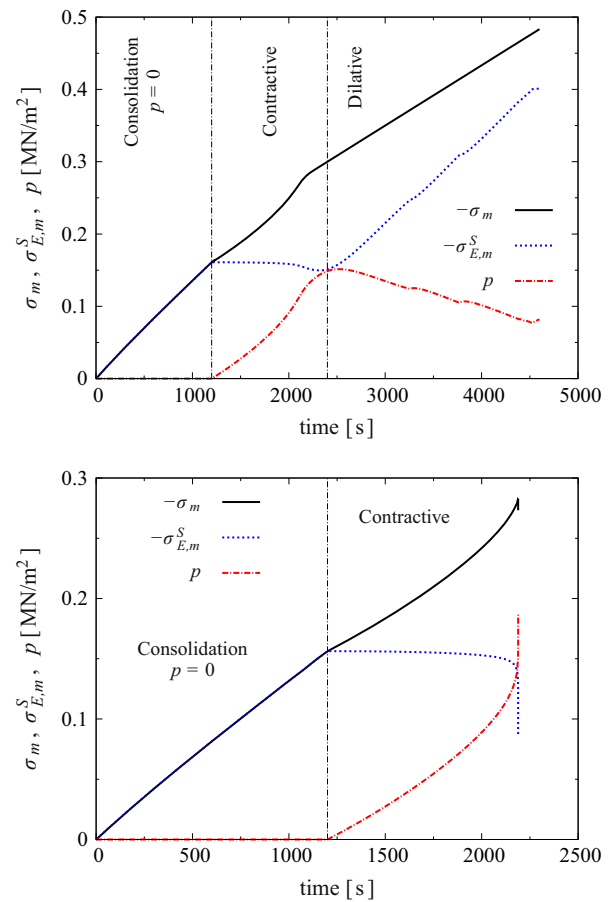


Fig. 7. Effective stress and pore pressure changes in undrained triaxial compression tests for case (3) of moderate-dense sand (top), and for case (4) of very loose sand (bottom).

is increasingly carried by the effective stress, whereas the pore pressure dissipates. Fig. 7, bottom, shows how the effective stress reduces and the pore pressure increases until the flow liquefaction takes place. When the mean effective stress tends towards zero, the whole applied stress is only carried by the pore fluid.

Under cyclic loading, saturated sand undergoes liquefaction with patterns similar to that observed under monotonic loading, cf., e.g., [48,49]. Employing the elasto-viscoplastic constitutive model as introduced in Section 3 with isotropic hardening, it is possible to follow the excess pore-pressure development and the onset of liquefaction events under cyclic loading. If the unloading–reloading process is carried out inside the yield surface, the response is governed by the hyperelastic material law. In this case, the reloading process follows the same path as the unloading process and only oscillatory but not accumulative pore-pressure behavior can be detected. When the stress state is found on the yield surface in both the compression and the extension sides, then a plastic volumetric strain and with that accumulation of the pore-pressure takes place, see [46] for more details and applications.

6. Factors influencing the dynamic response of saturated granular media

In the following, a number of important factors that affect the response of saturated porous media under dynamic loading are discussed. Those factors are tested on an IBVP that leads to a plastic strain localization under plane strain conditions. All computations

are carried out with the coupled FE solver PANDAS.⁵ The geometry and the boundary conditions of this problem are illustrated in Fig. 8, and the balance relations are the coupled PDE describing a biphasic medium with materially incompressible constituents.

Moreover, the considered solid skeleton response is elasto-viscoplastic with isotropic hardening (Section 3). The material parameters of the materially incompressible constituents are given in Tables A2 and A4 and only the case of a very loose sand (case (4) in Table A3) is taken into account. The first step in the problem is to apply an isotropic consolidation with $\sigma_{11} = \sigma_{22} = 100$ kPa. The consolidation is carried out very slowly and with drained top boundary ($p = 0$) so that no accumulation in the pore pressure can occur. To examine the effect of the loading rate, a fast (dynamic) or a slow (quasi-static) displacement, as illustrated in Fig. 9, is applied in the second step to the top of the domain until abort of the calculation (the same convergence criterion is used in all cases).

The influence of the boundary drainage is tested by varying the drainage of the top boundary under dynamic loading conditions. Additionally, the effect of the microstructure on the response is examined by using different values of the hydraulic permeability parameter k^f .

In the literature, many publications have discussed numerically and experimentally strain-localization problems and the factors affecting the formation of shear bands, such as the boundary conditions of the problem, the loading rate, the saturation, the density of sand and the size of the finite element mesh, see, e.g. [1,41,50,53,65]. Moreover, strain-localization and shear-band occurrence in fluid-saturated loose sand under deviatoric stress is a ‘deformation–diffusion problem’, where the effects of the pore-pressure development and the pore–fluid flow on the contraction/dilation of the solid matrix have to be taken into account. It has been shown in [1] that unlike the case of dense sand, where dilative shear bands appear, compactive shear bands occur in loose sand. Due to the coupled volumetric deformation–fluid-flow behavior, the compactive shear band initially looks less localized and diffused, which agrees well with the results of the presented problem. The discussion of shear bands is, however, a very diverse topic and beyond the scope of this study.

6.1. Loading rate effect: quasi-static vs. dynamic

Most factors influencing soil behavior are equally important under both dynamic and quasi-static loading conditions. However, the significant character of the dynamic behavior is the inertia force, which cannot be neglected and its importance increases with the increase of the loading speed. To understand the dependency of liquefaction occurrence on the rate of the applied displacement (dynamic or quasi-static), the problem introduced in Fig. 8 is analyzed considering the displacement loads depicted in Fig. 9. Therein, the velocity of the applied displacement is $\bar{v}_a = \dot{\bar{u}}_{S2} = -1.0 \times 10^{-2}$ m/s in the dynamic case and $\bar{v}_b = \dot{\bar{u}}_{S2} = -1.0 \times 10^{-6}$ m/s in the quasi-static case.

Fig. 10 shows exemplary contour plots of the computed vertical displacement u_{S2} , excess pore-pressure p and plastic volumetric strain ϵ_{Sp}^V under dynamic loading and top permeable boundary. Here, the pore-pressure build-up is accompanied with the plastic volumetric strain (permanent contraction tendency of loose sand), which indicates the probable location of the flow liquefaction event. Under the same boundary conditions except for the applied loading rate, which is now quasi-static, Fig. 11 shows a similar plastic volumetric strain distribution as in Fig. 10. However, a different pore-pressure distribution is obtained. This is because

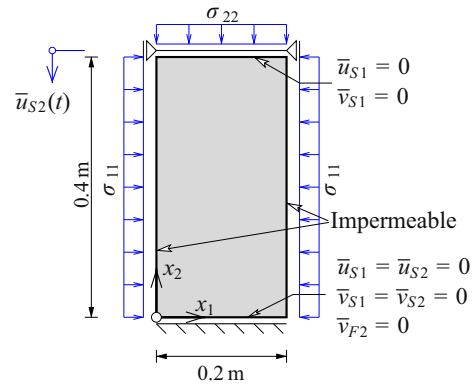


Fig. 8. Geometry and boundary conditions of the strain localization problem. Two cases for the top boundary are considered: B (1) with permeable top boundary ($\bar{p} = 0$) and B (2) with impermeable top boundary ($\bar{v}_{F2} = 0$).

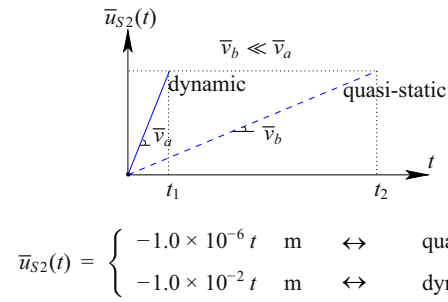


Fig. 9. Applied displacements of the strain localization problem.

under quasi-static conditions, the excess pore pressure at a certain point has the time to dissipate through the drained boundary (top boundary) or into neighboring regions of less accumulated pore pressure.

6.2. Boundary drainage effect

Fig. 12 shows contour plots of the computed vertical displacement u_{S2} , excess pore-pressure distribution p and plastic volumetric strain ϵ_{Sp}^V under dynamic loading condition and top impermeable boundary ($\bar{v}_{F2} = 0$). It is obvious from comparing Fig. 10 with Fig. 12 that the top impermeable specimen under dynamic loading behaves almost the same as the top permeable specimen under dynamic conditions. However, a shift in the volumetric plastic strain and the excess pore-pressure regions can be observed due to the top boundary drainage.

6.3. Influence of the microstructure

The microstructure of a granular material affects the liquefaction susceptibility in different ways. For instance, grain sizes play an important role in the response patterns, where fine and uniform sands are believed to be more liquefaction prone than coarse sands, cf. [69]. Another factor, which is related to the microstructure, is the length of the micro-channels with respect to the pore diameter. Here, under quickly-applied loading the long drainage path causes the specimens to behave almost like under perfectly undrained conditions. In the considered macroscopic modeling, the microtopology information of the granular material is included in the permeability parameter. Consequently, the liquefaction susceptibility increases by decreasing the value of the permeability parameter.

⁵ Porous media Adaptive Nonlinear finite element solver based on Differential Algebraic Systems, see <http://www.get-pandas.com>.

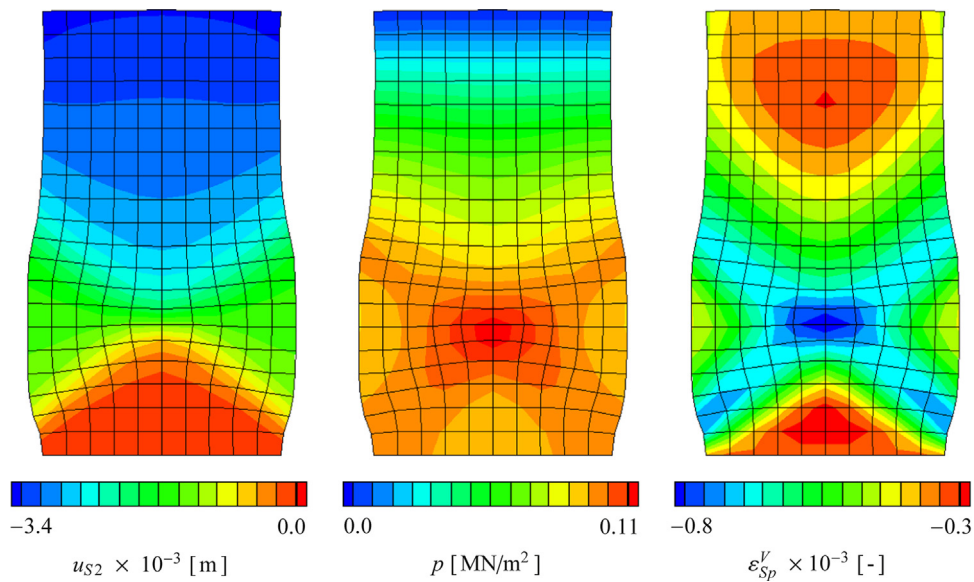


Fig. 10. Vertical displacement u_{S2} , excess pore pressure p and plastic volumetric strain ϵ_{Sp}^V for a very loose sand with top permeable boundary at $t = 0.34$ s. The applied deformation is dynamic according to Fig. 9 and $k^F = 10^{-6}$ m/s (deformed mesh scaled by a factor of 10).

Back to the numerical example in Fig. 8, two cases under the same applied dynamic loading but different permeability parameters are compared. Fig. 13 shows contour plots of the computed quantities u_{S2} , p and ϵ_{Sp}^V with top permeable boundary and permeability parameter $k^F = 10^{-2}$ m/s.

Comparing Fig. 13 with the lower permeability case ($k^F = 10^{-6}$ m/s) in Fig. 10, where all the other boundary conditions and parameters are the same, shows that no significant region for the accumulated pore pressure can be seen in Fig. 13. This is because under higher permeability, the pore fluid can easily escape from the domain.

7. Structure found on stratified liquefiable soil

In the following, a two-dimensional computational model of a soil–structure system under plane strain conditions is analyzed using the FE package PANDAS. The seismic excitation appears in the form of vertically incident shear waves, which is applied at the bottom of the profile, i.e., along the soil–bedrock interface boundary. The data of the seismic excitation in this example are based on realistic measurements, which are related to the Kobe earthquake,⁶ FUK station, horizontal north–south (NS) motion. These data are taken from the strong motion database of the Pacific Earthquake Engineering Research Center (PEER),⁷ which are freely available online for engineering applications. The geometry and the boundary conditions are illustrated in Fig. 14.

The chosen soil layers of the considered problem provide an appropriate environment to liquefaction events. Here, the present layers are illustrated in Fig. 14 and can briefly be demonstrated as follows: (1) A clayey silt surface layer, which is replaced in the numerical model by a uniformly distributed load (50.0 kN/m²). This layer provides permeable upper boundaries during the consolidation and the excess pore-pressure dissipation phases. (2) A liquefiable sand layer (10 m thick) on which the structure is installed. The expected behavior of this layer is nonlinear elastoplastic. Therefore, it is modeled

using the elasto-viscoplastic constitutive model with isotropic hardening as introduced in Section 3. Here, in order to capture the two significant liquefaction events of flow liquefaction and cyclic mobility, the parameters in Table A3 for very loose and moderate-dense sands are exploited. (3) A stiff clay layer (10 m thick) under the sand layer, which is characterized by a low permeability parameter and assumed to have a linear elastic response. If, instead, an elasto-viscoplastic material model is used, large plastic strains would occur in this layer as the seismic load is applied at its bottom, which makes the visualization of the plastic strains in the upper sandy layer under the structure of a difficult task. (4) A bedrock, at which the seismic load is applied, marks the bottom boundary of the considered IBVP.

In the current treatment, the modeling of soil proceeds from saturated, materially incompressible solid–fluid aggregates. Moreover, the domain of the boundary-value problem is chosen sufficiently wide in order to avoid the influence of the lateral boundaries on the response of the region of interest under the structure. The loading steps during the whole numerical treatment are illustrated in Fig. 15. The structure is assumed to be made of a very stiff material, e.g. concrete with material parameters given in Table 2, which can be approximated by a single-mass oscillator. Here, depending on the nature of the foundation soil, the structure might undergo settlement, uplifting, or overturning as will be discussed throughout this example. The parameters of the elasto-viscoplastic sand layer are given in Tables A2 and A4 with $k^F = 10^{-5}$ m/s, whereas the parameters of the elastic, stiff clay layer are presented in Table A1 with $k^F = 10^{-8}$ m/s.

As the aim of the following problem is to reveal the flow liquefaction and the cyclic mobility in saturated soils under extreme dynamic loadings and not to model a particular seismic event, the given earthquake excitation (the velocity time history in our case) is multiplied by amplification factors in order to get a clear and full soil response. In particular, two cases of the initial density and amplification factors are considered for the sand layer under the structure: firstly, for the case of flow-liquefaction-prone very loose sand, the seismic excitation is multiplied by a factor of 15. Secondly, for the case of moderate-dense sand, the earthquake data is magnified by a factor of 20 to manifest the cyclic mobility behavior. In the IBVP, the earthquake velocity time history is used as input data, which is compatible with the structure of the governing balance relations. Moreover, an implicit monolithic time-stepping algorithm using the Backward Euler (BE) scheme is exploited to solve the problem.

⁶ The Kobe earthquake took place in Japan in 1995 with a magnitude of approx. 7.2 on the Richter Scale.

⁷ The PEER website [<http://peer.berkeley.edu/smcat>] provides a large variety of reviewed and processed earthquake records, which are useful for engineering applications.

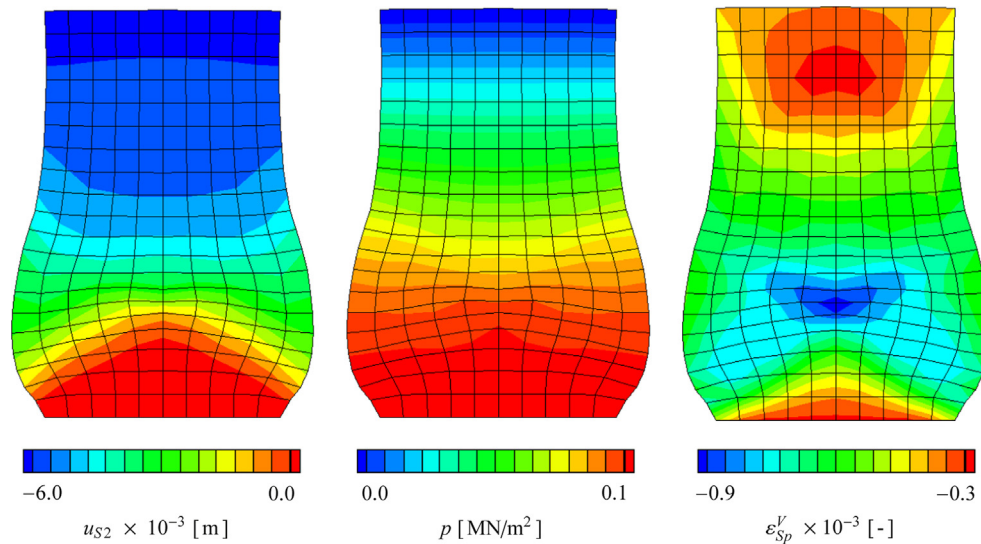


Fig. 11. Vertical displacement u_{S2} , excess pore-pressure p and plastic volumetric strain ϵ_{Sp}^V for a very loose sand with top permeable boundary at $t = 6000$ s. The applied deformation is quasi-static according to Fig. 9 and $k^F = 10^{-6}$ m/s (deformed mesh scaled by a factor of 10).

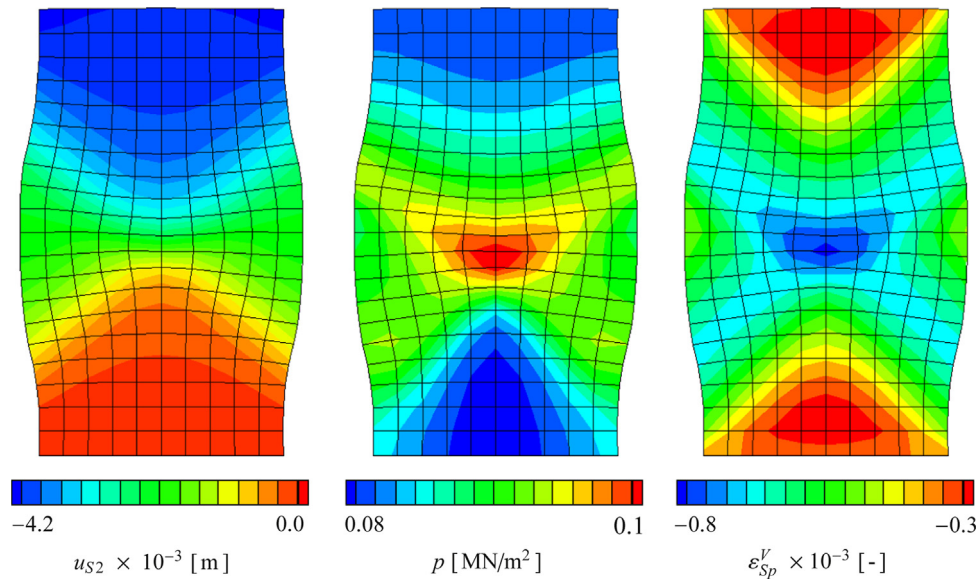


Fig. 12. Vertical displacement u_{S2} , excess pore-pressure p and plastic volumetric strain ϵ_{Sp}^V for a very loose sand with top impermeable boundary at $t = 0.42$ s. The applied deformation is dynamic according to Fig. 9 and $k^F = 10^{-6}$ m/s (deformed mesh scaled by a factor of 10).

7.1. Flow liquefaction in a very loose sand

Starting with the case of a very loose sand layer, Fig. 16 shows exemplary contour plots of the solid plastic volumetric strain evolution ϵ_{Sp}^V . This type of soil collapse is known as seismic-induced flow liquefaction, which leads to a punching shear failure in the loose foundation soil.⁸ Unlike the perfectly undrained

⁸ Bearing capacity failure happens when the shear stresses in the soil exceed its shear strength. Herein, depending on the foundation soil properties, three modes of bearing capacity failure can be recognized, cf. [15]: (1) *Punching shear failure* which usually occurs in loose foundation soils. In this case, no general shear surface is generated and the main deformations happen in the soil directly below the structure's footing. (2) *Local shear failure* which is normally seen in soils of medium dense nature. This type of failure is an intermediate state between punching and general shear collapse, where a partial shear surface can be distinguished immediately below the footing. (3) *General shear failure* usually happens in soils of dense or hard state and involves total rupture of the soil with a continuous and distinct shear surface.

CU triaxial tests, the behavior in the considered IBVP is partially undrained with possible excess pore-pressure dissipation during and after the dynamic loading. Herein, the excess pore pressure firstly accumulates in certain sand zones with high plastic volumetric strain and then migrates due to the pore-pressure gradient into neighboring zones of lower accumulated pore pressure. In this regard, Fig. 17 shows exemplary time sequence contour plots of the excess pore-water pressure p with deformed mesh (scaled by a factor of 10).

Following this, one distinguishes between the oscillatory pore pressure that appears in the elastic clay layer and the accumulative pore pressure in the sand layer under the foundation. In the latter, it is clear that the development of the plastic volumetric strain in certain zones coincides with the pore-pressure build-up. The interplay between the mean effective stress and the pore pressure at point B (2, 2) in the soil domain is depicted in Fig. 18, top. Herein, it is shown that the flow liquefaction takes place due to the reduction of the mean effective stress and build-up of the pore

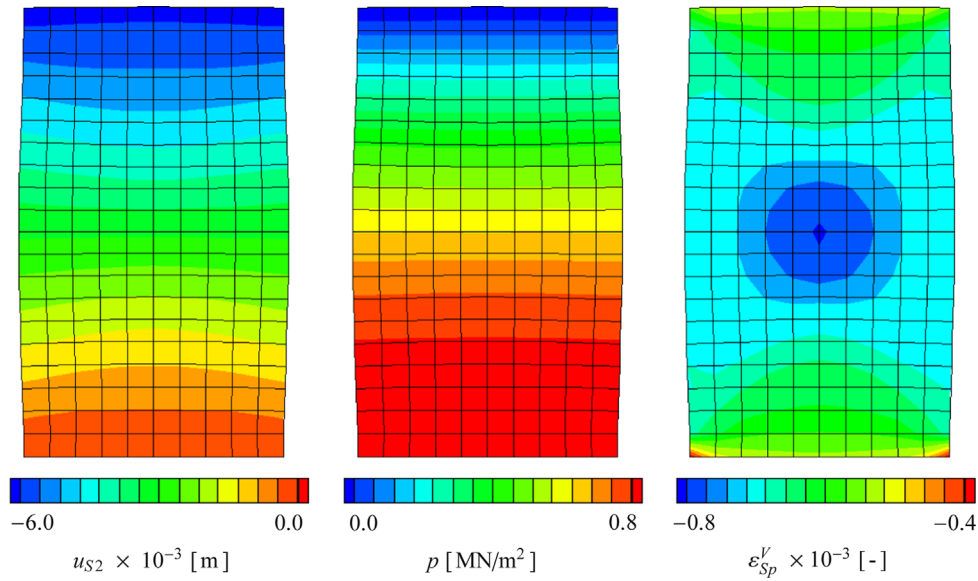


Fig. 13. Vertical displacement u_{S2} , excess pore-pressure p and plastic volumetric strain ϵ_{Sp}^V for a very loose sand with top permeable boundary at $t = 0.6$ s. The applied deformation is dynamic according to Fig. 9 and $k^f = 10^{-2}$ m/s (deformed mesh scaled by a factor of 10).

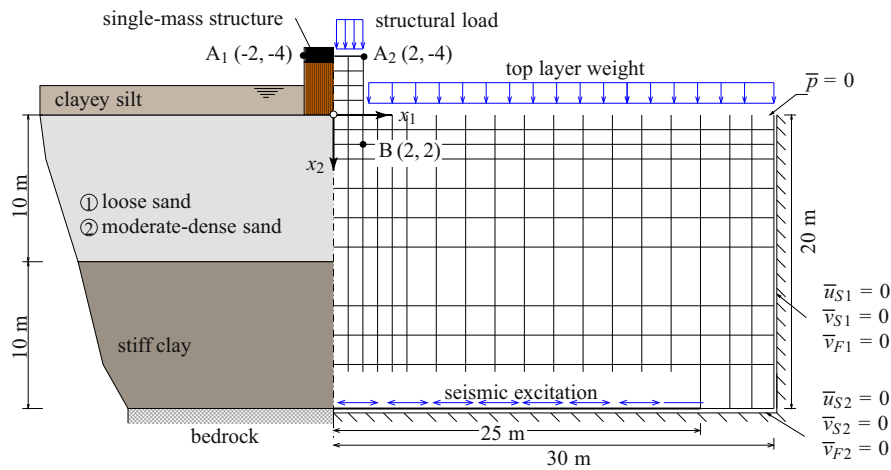


Fig. 14. Geometry and boundary conditions of the soil–structure interaction problem under seismic loading.

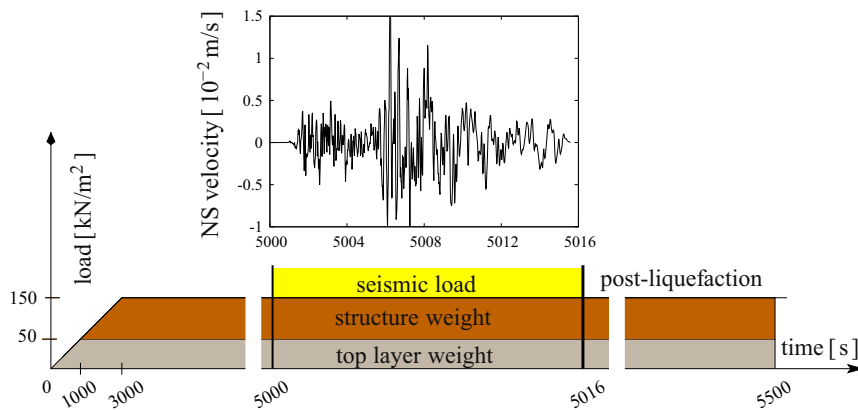


Fig. 15. Applied loads to the soil–structure interaction problem.

pressure until most of the applied stress is carried by the pore fluid (σ_E^z tends to zero). Moreover, the fast increase of the pore pressure at a certain stage of the loading is accompanied by a drastic

increase of the plastic volumetric strain in the soil. In particular, the continuous increase of the pore-water pressure under deviatoric stress conditions is associated with a contraction

Table 2
Material parameters of the linear elastic concrete.

Parameter	Symbol	Value	SI unit
1st Lamé constant of φ^S	μ^S	1.25×10^{10}	N/m ²
2nd Lamé constant of φ^S	λ^S	8.3×10^9	N/m ²
Effective solid density	ρ^{SR}	2800	kg/m ³
Initial solidity	n_{0s}^S	0.99	–
Darcy permeability	k^F	10^{-6}	m/s

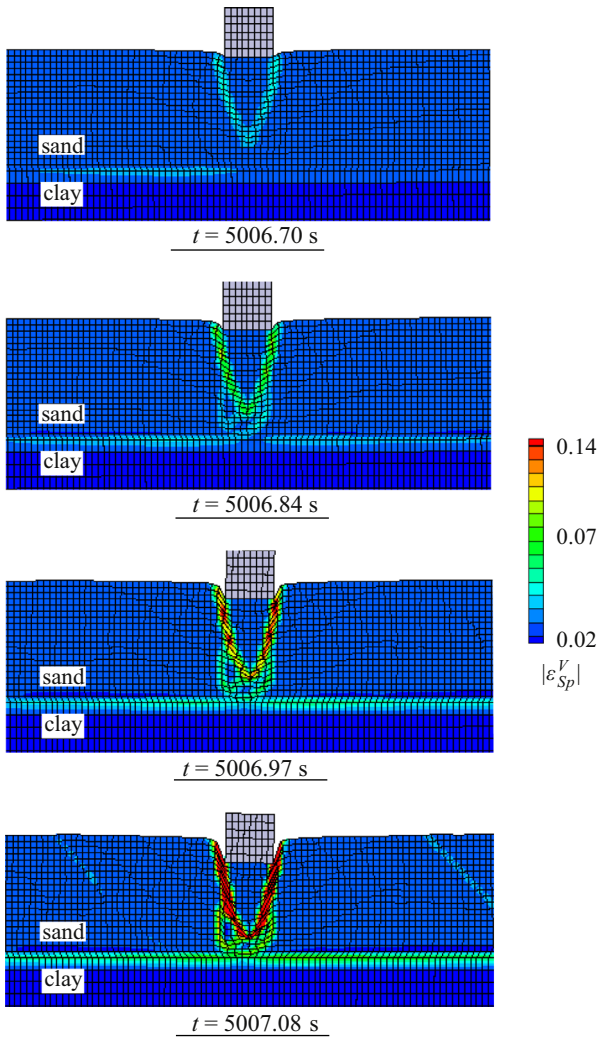


Fig. 16. Time sequence of solid plastic volumetric strain contour plots for the case of a very loose saturated sand layer under the structure (mesh deformation scaled by a factor of 10).

tendency of the loose sand layer ($\epsilon_{Sp}^V < 0$), cf. Fig. 18, bottom. Fig. 19 illustrates how the structure undergoes vertical as well as horizontal deformations during the seismic excitation. Shortly before the collapse, a rapid increase of the horizontal and the vertical deformations as well as a small inclination of the structure can be observed.

It is worth mentioning that in the case of a very loose foundation sand layer with magnified seismic excitation by a factor of 15, the flow liquefaction takes place during the earthquake excitation and leads to relatively large deformations, and

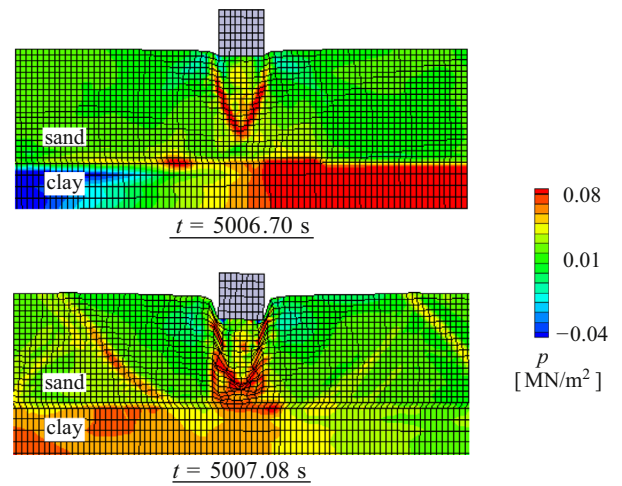


Fig. 17. Time sequence of pore pressure contour plots for the case of a very loose soil layer under the foundation (mesh deformation scaled by a factor of 10).

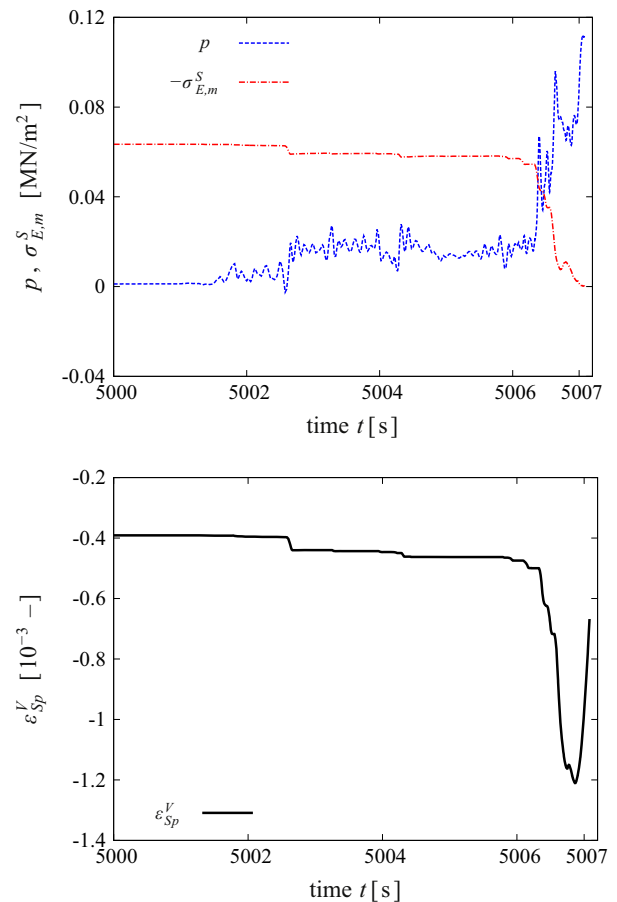


Fig. 18. Pore pressure and mean effective stress time history at B (2, 2) (top), and solid plastic volumetric strain time history at point B (bottom) during the seismic excitation, case (1).

thus, the numerical calculation terminates before the post-liquefaction (dissipation) phase, cf. Fig. 15.

7.2. Cyclic mobility in a moderate-dense sand

For a moderate-dense sand layer under the structure, Fig. 20 shows exemplary contour plots of the solid plastic volumetric

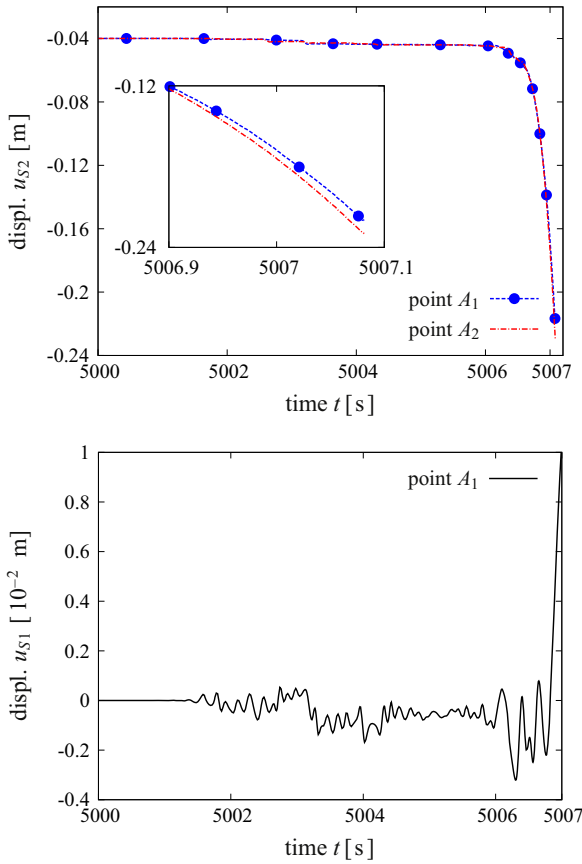


Fig. 19. Vertical displacement time history at points A_1 (−2, −4) and A_2 (2, −4) (top), and horizontal displacement time history at point A_1 (bottom) during the seismic excitation, case (1).

strain evolution ϵ_{Sp}^V at different times during the earthquake loading. The behavior in Fig. 20 represents the seismically induced cyclic mobility, where a limited accumulation of the pore pressure takes place and the effective stress can never reach a zero value. In this connection, Fig. 21, top, depicts the interplay between the effective stress and the pore pressure at point B (2, 2) during the application of the seismic excitation. Here, a slight build-up of the pore-water pressure can be seen till $t \approx 5004$ s, which is followed by a decrease of the pore pressure and an increase in the mean effective stress. Fig. 21, bottom, shows that an immense increase in the solid plastic volumetric strain ($\epsilon_{Sp}^V > 0 \rightarrow$ dilative) occurs when the seismic excitation reaches its peak value at $t \approx 5006.6$ s causing a clear plastic shear strain failure line under the structure (cf. Fig. 20).

Fig. 22, top, depicts the vertical displacement time history at points A_1 (−2, −4) and A_2 (2, −4) at the top of the structure. It is clear that the vertical settlement in the case of moderate-dense sand is less than that in the very loose sand layer case. Moreover, at the end of the earthquake loading, a small inclination of the structure can be observed. Fig. 22, bottom, shows the horizontal motion of the structure during the seismic excitation. Here, a residual horizontal displacement can be detected at the end of the dynamic loading.

8. Conclusions

In this paper, the modeling of materially incompressible, fluid-saturated porous media within a continuum-mechanical

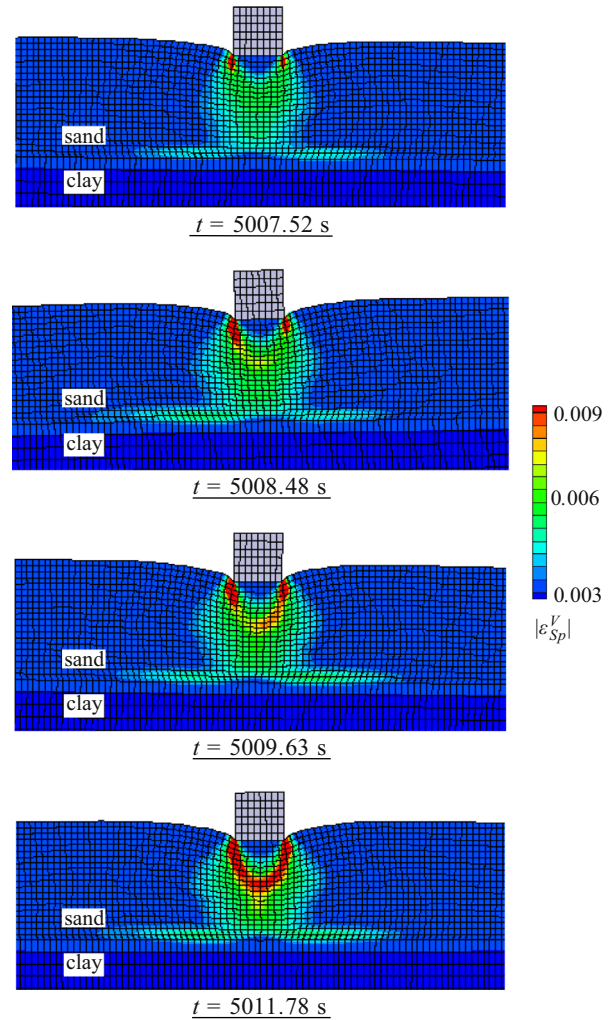


Fig. 20. Time sequence of the solid plastic volumetric strain ϵ_{Sp}^V contour plots for a moderate-dense saturated sand layer under the structure (deformed mesh scaled by a factor of 30).

framework has been investigated. For this, thermodynamically consistent material models were used and a special attention has been paid to the behavior under dynamic loading conditions. This enabled us to understand and simulate important events in porous media dynamics, such as liquefaction phenomena.

The macroscopic material modeling was carried out by exploiting the Theory of Porous Media (TPM). Moreover, the treatment proceeded from saturated biphasic solid-fluid aggregates and was committed to the isothermal and geometrically linear scope. Regarding the constitutive modeling, the material response of the solid skeleton for the simulation of liquefaction-related phenomena was considered elasto-viscoplastically. This entailed the implementation of a hyperelastic model for the nonlinear elastic behavior and the exploitation of a single-surface yield function for modeling the plastic solid response.

The continuum-mechanical treatment of multiphase materials yields a volume-coupled formulation with the coupling inherent in the governing conservation laws. To solve initial-boundary-value problems of porous media dynamics in this work, the governing PDE, basically the solid and fluid momentum balances and the overall mass balance, were firstly discretized in space using the FEM and secondly in time using the monolithic implicit (Backward) Euler time-integration strategy. This way of treatment

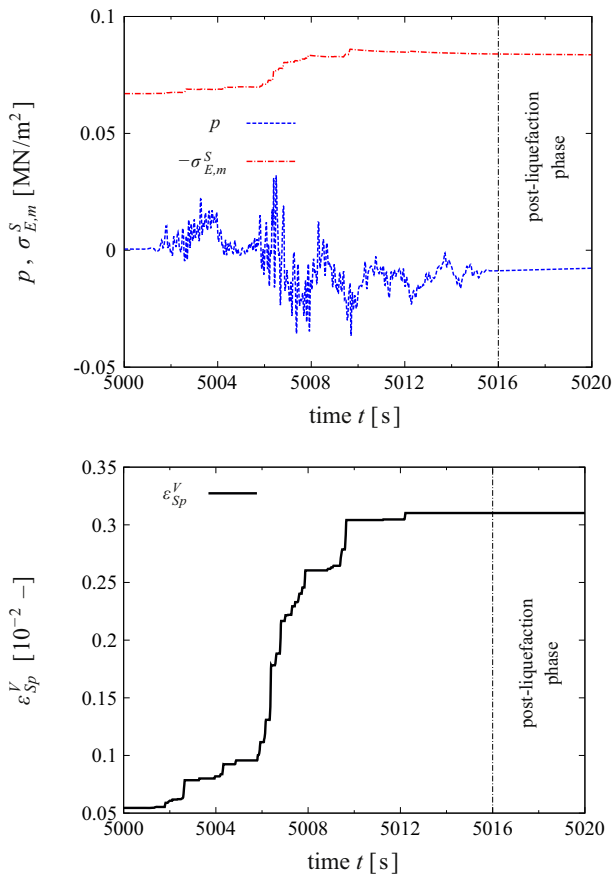


Fig. 21. Pore-pressure and mean effective stress time history at point B (2, 2) (top), and solid plastic volumetric strain time history at B (bottom) during the seismic excitation and post-liquefaction for case (2) of moderate-dense sand.

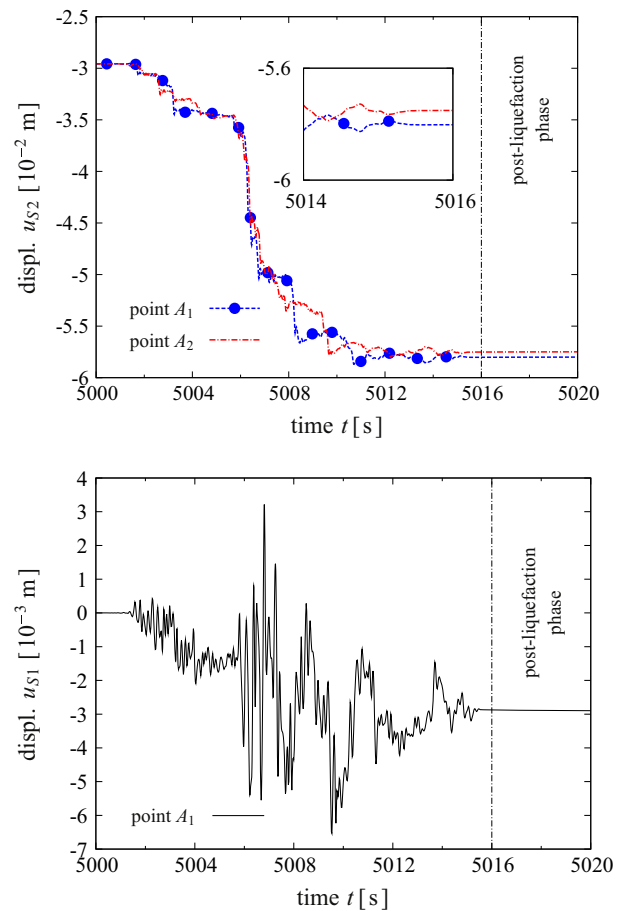


Fig. 22. Vertical displacement time history at points A_1 (-2, -4) and A_2 (2, -4) (top), and horizontal displacement time history at point A_1 (bottom) for case (2) of moderate-dense sand.

led to stable and robust solutions, provided that stable mixed finite elements are used.

A considerable part of this paper was devoted to the investigation of liquefaction phenomena, which usually appear in saturated granular materials after dynamic excitation. This included the definitions and the description of liquefaction mechanisms, such as the pore-fluid pressure accumulation and softening of the granular structure, and factors influencing saturated soil behavior. Under drained conditions, the volumetric strain is used as an indicator for the contractive and the dilative behavior. However, under undrained conditions, the contraction tendency leads to a pore-pressure accumulation and a change in the mean effective stress, which is governed by the principle of effective stresses. The response of granular materials depends very much on the initial density and leads to two significant physical events, which are the ‘flow liquefaction’ and the ‘cyclic mobility’.

The aforementioned features have been numerically captured by applying the considered elasto-viscoplastic model to initial-boundary-value problems of saturated soil dynamics in the two-dimensional space. Therefore, it is very interesting for future implementations to consider three-dimensional problems together with parallel computation using commercial FE codes. In this regard, a powerful scripting environment for monolithic time integrations can be achieved by

introducing a linking interface between the coupled FE solver PANDAS and the ABAQUS commercial FE package, see [35,72].

The presented investigation can serve as a base for future studies and applications in the fields of porous media dynamics and soil–structure interaction. In this, the methods and constitutive models to describe coupled solid-fluid problems can successfully be used to simulate important phenomena in saturated porous materials, such as different wave propagation and liquefaction events. Furthermore, the discussed numerical strategies and algorithms provide a good understanding of the solution behavior and detailed steps for practical applications.

Appendix A. Material parameters

The material parameters that enter the elasto-viscoplastic model have been identified based on triaxial experiments, conducted at the Institute of Applied Mechanics, University of Stuttgart. For details about the different experiments and the parameter identification and optimization strategies, the reader is referred to the works by, e.g., [32,36,63,73] (Tables A1–A4).

Table A1
Material parameters of the linear elastic solid skeleton response.

Parameter	Symbol	Value	SI unit
1st Lamé constant of φ^S	μ^S	5.583×10^6	N/m ²
2nd Lamé constant of φ^S	λ^S	8.375×10^6	N/m ²
Effective solid density	ρ^{SR}	2000	kg/m ³
Effective fluid density	ρ^{FR}	1000	kg/m ³
Initial solidity	n_{0S}^S	0.67	–
Darcy permeability	k^F	10^{-8}	m/s

Table A2
Material parameters of the nonlinear hyperelastic solid matrix.

Parameter	Symbol	Value	SI unit
1st Lamé constant of φ^S	μ^S	150×10^6	N/m ²
Initial bulk modulus of φ^S	k_0^S	28×10^6	N/m ²
Nonlinear bulk modulus of φ^S	k_1^S	43×10^6	N/m ²
Effective solid density	ρ^{SR}	1550	kg/m ³
Effective pore fluid density	ρ^{FR}	1000	kg/m ³
Initial volume fraction of φ^S	n_{0S}^S	0.585	–
Max. volume fraction of φ^S	n_{max}^S	0.595	–

Table A3
Sand with different initial densities (classifications according to the relative density $Dr := (n_{0S}^S - n_{min}^S) / (n_{max}^S - n_{min}^S) \times 100\%$, cf. [62]), which requires different plastic potential parameters.

Case	n_{0S}^S	n_{max}^S	n_{min}^S	Dr (%)	ψ_1	ψ_2
(1)	0.585	0.595	0.38	95	1.1	0.64
(2)	0.5	0.595	0.38	56	0.5	0.5
(3)	0.45	0.595	0.38	33	0.5	0.3
(4)	0.4	0.595	0.38	9.5	0.4	0.1

Table A4
Parameters of the viscoplasticity model: basic viscoplasticity parameters P (1), plastic potential dilatancy parameters P (2), initial values of the hardening/softening plasticity parameters P (3), the final values P (4), the volumetric isotropic hardening P (5), and the deviatoric isotropic hardening P (6).

Parameter	Symbol	Sand (1)	Sand (2)	SI unit
P (1)	α	0.01	0.01	–
	κ	0.1×10^3	2.0×10^3	m ² /N
	m	0.5454	0.5454	–
	η_r	10^{-3}	10^{-3}	s
	r	1.5	1.5	–
	σ_0	0.1×10^3	2.0×10^3	N/m ²
	P (2)	ψ_1	0.97	0.4/0.5
ψ_2		0.48	0.1/0.3	–
P (3)	δ_0	0.01×10^{-6}	0.008×10^{-6}	m ² /N
	ϵ_0	0.081×10^{-6}	0.01×10^{-6}	m ² /N
	β_0	0.105	0.11	–
	γ_0	0.0	0.0	–
P (4)	δ^*	0.005×10^{-6}	0.005×10^{-6}	m ² /N
	ϵ^*	0.008×10^{-6}	0.0135×10^{-6}	m ² /N
	β^*	0.263	0.0	–
	γ^*	1.6	1.6	–
P (5)	C_δ^V	-100×10^{-6}	-90×10^{-6}	–
	C_ϵ^V	-300×10^{-6}	-300×10^{-6}	–
	C_β^V	-58	-58	–
	C_γ^V	-10	-10	–

Table A4 (continued)

Parameter	Symbol	Sand (1)	Sand (2)	SI unit
P (6)	C_δ^D	25×10^{-6}	15.9×10^{-6}	–
	C_ϵ^D	300×10^{-6}	300×10^{-6}	–
	C_β^D	350	350	–
	C_γ^D	35	35	–

References

- Andradea J, Borja RI. Modeling deformation banding in dense and loose fluid-saturated sands. *Finite Elem Anal Des* 2007;43:361–83.
- Arnold DN. Mixed finite element methods for elliptic problems. *Comput Methods Appl Mech Eng* 1990;82:281–300.
- Ascher UM, Petzold LR. *Computer methods for ordinary differential equations and differential-algebraic equations*. U.S.: Society for Industrial & Applied Mathematics; 1998.
- Avci O, Ehlers W. Stress-dependent failure surface of granular materials. *Proc Appl Math Mech* 2010;8:10401–2.
- Biot MA. General theory of three-dimensional consolidation. *J Appl Phys* 1941;12:155–64.
- Biot MA. Theory of propagation of elastic waves in a fluid-saturated porous solid, I. Low frequency range. *J Acoust Soc Am* 1956;28:168–78.
- Biot MA. Theory of propagation of elastic waves in a fluid-saturated porous solid, II. Higher frequency range. *J Acoust Soc Am* 1956;28:179–91.
- Bowen RM. Theory of mixtures. In: Eringen AC, editor. *Continuum physics, mixtures and EM field theories*, vol. 3. London: Academic Press; 1976. p. 1–127.
- Bowen RM. Incompressible porous media models by use of the theory of mixtures. *Int J Eng Sci* 1980;18:1129–48.
- Bowen RM. Compressible porous media models by use of the theory of mixtures. *Int J Eng Sci* 1982;20:697–735.
- Breuer S. Quasi-static and dynamic behavior of saturated porous media with incompressible constituents. *Transp Porous Media* 1999;34:285–303.
- Brezzi F, Fortin M. *Mixed and hybrid finite element methods*. New York: Springer-Verlag; 1991.
- Castro G. On the behavior of soils during earthquakes liquefaction. In: Cakmak AS, editor. *Soil dynamics and liquefaction*. Amsterdam: Elsevier Science Publication; 1987. p. 169–204.
- Coussy O. *Mechanics of porous continua*. Chichester: Wiley; 1995.
- Day RW. *Geotechnical earthquake engineering handbook*. New York: McGraw-Hill; 2002.
- deBoer R. *Theory of porous media*. Berlin: Springer-Verlag; 2000.
- deBoer R. *Trends in continuum mechanics of porous media. Theory and applications of transport in porous media*, vol. 18. Dordrecht, The Netherlands: Springer; 2005.
- deBoer R, Ehlers W. Theorie der Mehrkomponentenkontinua mit Anwendung auf bodenmechanische Probleme. *Forschungsberichte aus dem Fachbereich Bauwesen, Heft 40*, Universität-GH-Essen; 1986.
- deBoer R, Ehlers W. The development of the concept of effective stresses. *Acta Mech* 1990;83:77–92.
- deGroot MB, Bolton MD, Foray P, Meijers P, Palmer AC, Sandven R, et al. Physics of liquefaction phenomena around marine structures. *J Waterw Port Coast Ocean Eng* 2006;132:227–43.
- di Prisco C, Imposimato S. Nonlocal numerical analyses of strain localisation in dense sand. *Math Comput Model* 2003;37:497–506.
- Diebels S, Ehlers W. Dynamic analysis of a fully saturated porous medium accounting for geometrical and material non-linearities. *Int J Numer Methods Eng* 1996;39:81–97.
- Diebels S, Ehlers W, Markert B. Neglect of the fluid extra stresses in volumetrically coupled solid-fluid problems. *Z Angew Math Mech* 2001;81:521–2.
- Drumheller DS. The theoretical treatment of a porous solid using a mixture theory. *Int J Solids Struct* 1978;14:441–56.
- Ehlers W. On thermodynamics of elasto-plastic porous media. *Arch Mech* 1989;41:73–93.
- Ehlers W. Toward finite theories of liquid-saturated elasto-plastic porous media. *Int J Plast* 1991;7:443–75.
- Ehlers W. An elastoplasticity model in porous media theories. *Transp Porous Media* 1992;9:49–59.
- Ehlers W. Constitutive equations for granular materials in geomechanical context. In: Hutter K, editor. *Continuum mechanics in environmental sciences and geophysics*. CISM courses and lecture notes no. 337. Wien: Springer-Verlag; 1993. p. 313–402.
- Ehlers W. A single-surface yield function for geomaterials. *Arch Appl Mech* 1995;65:246–59.
- Ehlers W. Foundations of multiphase and porous materials. In: Ehlers W, Bluhm J, editors. *Porous media: theory, experiments and numerical applications*. Berlin: Springer-Verlag; 2002. p. 3–86.

- [31] Ehlers W. Porose Medien - ein kontinuumsmechanisches Modell auf der Basis der Mischungstheorie. Reprint of the habilitation from the year 1989 (Forschungsberichte aus dem Fachbereich Bauwesen, Heft 47, Universität-GH-Essen), Report No. II-22 of the Institute of Applied Mechanics (CE), University of Stuttgart, Germany; 2012.
- [32] Ehlers W, Avcı O. Stress-dependent hardening and failure surfaces of dry sand. *Int J Numer Anal Methods Geomech* 2013;37:787–809.
- [33] Ehlers W, Ellsiepen P. Theoretical and numerical methods in environmental continuum mechanics based on the Theory of Porous Media. In: Schrefler BA, editor. *Environmental geomechanics*. CISM courses and lectures no. 417. Wien: Springer-Verlag; 2001. p. 1–81.
- [34] Ehlers W, Graf T, Ammann M. Deformation and localization analysis of partially saturated soil. *Comput Methods Appl Mech Eng* 2004;193:2885–910.
- [35] Ehlers W, Schenke M, Markert B. Liquefaction phenomena in fluid-saturated soil based on the theory of porous media and the framework of elastoplasticity. *ZAMM—J Appl Math Mech/Z Angew Math Mech*, <http://dx.doi.org/10.1002/zamm.201200220>; 2013.
- [36] Ehlers W, Scholz B. An inverse algorithm for the identification and the sensitivity analysis of the parameters governing micropolar elasto-plastic granular material. *Arch Appl Mech* 2007;77:911–31.
- [37] Eipper G. Theorie und Numerik finiter elastischer Deformationen in flüide-sättigten porösen Festkörpern. Dissertation, Bericht Nr. II-1, Institut für Mechanik (Bauwesen), Universität Stuttgart; 1998.
- [38] Ellsiepen P. Zeit- und ortsadaptive Verfahren angewandt auf Mehrphasenprobleme poröser Medien. Dissertation, Bericht Nr. II-3, Institut für Mechanik (Bauwesen), Universität Stuttgart; 1999.
- [39] Goodman MA, Cowin SC. A continuum theory for granular materials. *Arch Rat Mech Anal* 1972;44:249–66.
- [40] Gresho PM, Sani RL. *Incompressible flow and the finite element method*, vol. 2. Wiley, Chichester, second corrected reprint of 1998; 2000.
- [41] Guo P. Undrained shear band in water saturated granular media: a critical revisiting with numerical examples. *Int J Numer Anal Methods Geomech* 2013;37:353–73.
- [42] Hairer E, Wanner G. *Solving ordinary differential equations: stiff and differential-algebraic problems*, vol. 2. Berlin: Springer-Verlag; 1991.
- [43] Hassanzadeh SM, Gray WG. High velocity flow in porous media. *Transp Porous Media* 1987;2:521–31.
- [44] Haupt P. On the concept of an intermediate configuration and its application to a representation of viscoelastic-plastic material behavior. *Int J Plast* 1985;1:303–16.
- [45] Haupt P. *Continuum mechanics and theory of materials*. 2nd ed. Berlin: Springer-Verlag; 2002.
- [46] Heider Y. Saturated porous media dynamics with application to earthquake engineering. Dissertation, Report No. II-25 of the Institute of Applied Mechanics (CE), University of Stuttgart, Germany; 2012.
- [47] Heider Y, Markert B, Ehlers W. Dynamic wave propagation in infinite saturated porous media half spaces. *Comput Mech* 2012;49:319–36.
- [48] Ishihara K. *Soil behaviour in earthquake geotechnics*. New York: Oxford University Press Inc.; 1996.
- [49] Ishihara K, Tatsuoka F, Yasuda S. Undrained deformation and liquefaction of sand under cyclic stresses. *Solids Found* 1975;15(1):29–44.
- [50] Kimoto S, Oka F, Higo Y. Strain localization analysis of elasto-viscoplastic soil considering structural degradation. *Comput Methods Appl Mech Eng* 2004;193:2845–66.
- [51] Kolymbas D. An outline of hypoplasticity. *Arch Appl Mech* 1991;61:143–51.
- [52] Kramer SL, Elgamel AW. Modeling soil liquefaction hazards for performance-based earthquake engineering. A report on research, PEER 2001/13, The Pacific Earthquake Engineering Research Center (PEER); 2001.
- [53] Lade PV, Wang Q. Effect of boundary conditions on shear banding in true triaxial tests on sand. *Geotech Eng J SEAGS AGSSEA* 2011;42:19–25.
- [54] Lewis RW, Schrefler BA. *The finite element method in the static and dynamic deformation and consolidation of porous media*. 2nd ed. Chichester: Wiley; 1998.
- [55] Ling HI, Yue D, Kaliakin VN, Themelis NJ. Anisotropic elastoplastic bounding surface model for cohesive soils. *J Eng Mech* 2002;128:748–58.
- [56] Magda W. Wave-induced cyclic pore-pressure perturbation effects in hydrodynamic uplift force acting on submarine pipeline buried in seabed sediments. *Coast Eng* 2000;39:243–72.
- [57] Mahnkopf D. Lokalisierung flüidegesättigter poröser Festkörper bei finiten elastoplastischen Deformationen. Dissertation, Bericht Nr. II-5, Institut für Mechanik (Bauwesen), Universität Stuttgart; 2000.
- [58] Manzari MT, Dafalias YF. A critical state two-surface plasticity model for sands. *Géotechnique* 1997;47B:255–72.
- [59] Markert B. A biphasic continuum approach for viscoelastic high-porosity foams: comprehensive theory, numerics, and application. *Arch Comput Methods Eng* 2008;15:371–446.
- [60] Markert B. Weak or strong: on coupled problems in continuum mechanics. Habilitation, Report No. II-20, Institute of Applied Mechanics (CE), University of Stuttgart, <http://elib.uni-stuttgart.de/opus/volltexte/2010/5453/>; 2010.
- [61] Markert B, Heider Y, Ehlers W. Comparison of monolithic and splitting solution schemes for dynamic porous media problem. *Int J Numer Methods Eng* 2010;82:1341–83.
- [62] Moller G. *Geotechnik Bodenmechanik Bauingenieur-Praxis*. Berlin: Ernst & Sohn; 2007.
- [63] Müllerschön H. Spannungs-Verformungsverhalten granularer Materialien am Beispiel von Berliner Sand. Dissertation, Bericht Nr. II-6, Institut für Mechanik (Bauwesen), Universität Stuttgart; 2000.
- [64] Niemunis A. Extended hypoplastic models for soils. Habilitation, Report No. 34, Ruhr-Universität Bochum; 2002.
- [65] Oka F, Higo Y, Kimoto S. Effect of dilatancy on the strain localization of water-saturated elasto-viscoplastic soil. *Int J Solids Struct* 2002;39:3625–47.
- [66] Okamura M, Soga Y. Effects of pore fluid compressibility on liquefaction resistance of partially saturated sand. *Soils Found* 2006;46:695–700.
- [67] Pastor M, Zienkiewicz C, Chan AHC. Generalized plasticity and the modelling of soil behaviour. *Int J Numer Anal Methods Geomech* 1990;14:151–90.
- [68] Perzyna P. Fundamental problems in viscoplasticity. *Adv Appl Mech* 1966;9:243–377.
- [69] Prakash S. *Soil dynamics*. New York: McGraw-Hill; 1981.
- [70] Roscoe KH, Burland JB. On the generalized stress-strain behaviour of wet clay. In: Heyman J, Leckie FA, editors. *Engineering plasticity*. Cambridge, U.K.: Cambridge University Press; 1968. p. 535–609.
- [71] Schanz M, Diebels S. A comparative study of Biot's theory and the linear Theory of Porous Media for wave propagation problems. *Acta Mech* 2003;161:213–35.
- [72] Schenke M, Ehlers W. On the analysis of soils using an Abaqus-PANDAS interface. *Proc Appl Math Mech* 2011;11:431–2.
- [73] Scholz B. Application of a micropolar model to the localization phenomena in granular materials. Dissertation, Report No. II-15, Institute of Applied Mechanics (CE), University of Stuttgart; 2007.
- [74] Steeb H. Ultrasound propagation in cancellous bone. *Arch Appl Mech* 2010;80:489–502.
- [75] Steeb H, Frehner M, Schmalholz S. Waves in residual-saturated porous media. In: Maugin GA, Metrikine AV, editors. *Mechanics of generalized continua: one hundred years after the Cosserats*. New York, London: Springer; 2010. p. 179–90.
- [76] Truesdell C, Toupin RA. The classical field theories. In: Flügge S, editor. *Handbuch der Physik* Band, III/1. Berlin: Springer-Verlag; 1960. p. 226–902.
- [77] Verdugo R, Ishihara K. The steady state of sandy soils. *Soils Found* 1996;36(2):81–91.
- [78] Zienkiewicz OC, Chan AHC, Pastor M, Paul DK, Shiomi T. Static and dynamic behaviour of soils: a rational approach to quantitative solutions. I. Fully saturated problems. *Proc R Soc Lond* 1990;429:285–309.
- [79] Zienkiewicz OC, Chan AHC, Pastor M, Schrefler BA, Shiomi T. *Computational geomechanics with special reference to earthquake engineering*. Chichester: Wiley; 1999.
- [80] Zienkiewicz OC, Chang CT, Hinton E. Non-linear seismic response and liquefaction. *Int J Numer Anal Methods Geomech* 1978;2:381–404.
- [81] Zienkiewicz OC, Taylor RL. *The finite element method: the basis*, 5th ed. vol. 1. Oxford: Butterworth Heinemann; 2000.